



$^{40}\text{Ar}/^{39}\text{Ar}$ age constraints on the formation of fluid-rich quartz veins from the NW Rhenohercynian zone (Rursee area, Germany)

Akbar Aydin Oglu Huseynov^{1*}, Jan R. Wijbrans¹, Klaudia F. Kuiper¹ & Jeroen van der Lubbe¹

¹Vrije Universiteit Amsterdam, De Boelelaan 1085, 1081HV Amsterdam, the Netherlands

Correspondence to: Akbar Aydin Oglu Huseynov (a.huseynov@vu.nl)

Abstract. The late Palaeozoic Variscan orogeny (~350 Ma) dictates a significant part of the subsurface geology in north-western and central Europe. Our focus is particularly on veining that occurred in metamorphosed sedimentary rocks that are affected by this orogeny. Vein minerals serve as repositories for documenting the origin of subsurface fluid flows and dynamics, and dating them provides crucial insight into the timing of orogenic and possible reactivation events. The Rursee area (Rhenish Massif, Germany) that is part of the Variscan foreland zone on the Avalonia micro-continent represents a key locality for studying Variscan quartz vein formation. Based on structural grounds, the two different groups/types of Rursee quartz veins have been linked with the early stages of Variscan, but their absolute ages are still unknown.

The aim of this study is to date these quartz veins using the $^{40}\text{Ar}/^{39}\text{Ar}$ stepwise crushing method based on the radioactive decay of ^{40}K dissolved in high salinity fluid inclusions (FIs). We obtained Jurassic to Cretaceous ages, and the isotopic analysis of argon gases revealed that the fluid-rich quartz fractions release ^{39}Ar in two distinct phases. Regardless of quartz veins FIs salinity, stepwise crushing provides apparent $\text{K}/\text{Cl} > 1$. Electron Probe Micro Analyser data confirm the presence of the K (^{39}Ar) in the K-bearing mineral inclusions (e.g., sericite, mica, and chlorite) and in microcracks and possibly in the crystal lattice of quartz.

K-bearing mineral inclusions and/or crystal lattice of quartz, which form in the Variscan-origin vein fractures, provide a plausible explanation for the young apparent isotopic ages. The presence of the quartz sub-grains may suggest that obtained ages are likely to reflect post-Variscan reactivation-recrystallisation due to tectonic activity or its cooling moment during the Jurassic-Cretaceous period rather than the original Variscan vein formation.

This study emphasizes the complexities of isotopic dating of FIs, as well as the importance of careful interpretation of such data, especially in cases where different K-bearing mineral inclusions and/or radiogenic argon from crystal lattice obscure the initial FIs signal.

1 Introduction

Quartz veins are abundant in metamorphosed terranes and sedimentary basins filled with siliciclastic sediments, witnessing significant fluid movement during diagenesis and metamorphism (Yardley, 1983; Mullis et al., 1994; Cartwright & Buick, 2000; Oliver & Bons, 2001). Increase in both temperature and pressure during burial diagenesis, orogenesis and deformation



30 cause sedimentary and volcanic rocks to lose their volatile components and to release warm fluids, which cumulate minerals
31 in fractures and faults (Baumgartner & Ferry, 1991; Yardley & Bottrell, 1993; Oliver & Bons, 2001; Cox, 2007). These often
32 saline fluids contain, among others, $\text{KCl}_{(\text{aq})}$ or $\text{K}_2\text{CO}_3_{(\text{aq})}$ (Rauchenstein-Martinek et al., 2014), which are partly precipitated
33 during crystallisation of minerals in veins or as inclusions in these minerals (Sterner et al., 1988). One of the isotopes of
34 potassium, ^{40}K , is radioactive and can be used for K-Ar or its derivative $^{40}\text{Ar}/^{39}\text{Ar}$ dating. Progressive crushing techniques
35 enable to liberate gasses from fluid inclusions (FIs), mineral inclusions and/or crystal lattice for the age determination of
36 geological events provided that K-concentrations are high enough (Qiu & Dai, 1989; Turner & Bannon, 1992; Turner & Wang,
37 1992; Qiu, 1996; Kendrick et al., 2001; Qiu & Wijbrans, 2006; Kendrick et al., 2006; Qiu & Wijbrans, 2008; Qiu & Jiang,
38 2007; Jiang et al., 2012; Bai et al., 2013; Liu et al., 2015). This method does not only define an age, but also quantifies the
39 ratio of noble gases (e.g. $^{39}\text{Ar}_{\text{K}}/^{37}\text{Ar}_{\text{Ca}}$, $^{39}\text{Ar}_{\text{K}}/^{38}\text{Ar}_{\text{Cl}}$) derived from Ca, K and Cl, respectively, that have been formed during
40 neutron radiation prior to analysis. The $^{39}\text{Ar}_{\text{K}}/^{38}\text{Ar}_{\text{Cl}}$ provides important information on the composition of parental fluids and
41 their sources (Sumino et al., 2011; Cartwright et al., 2013). In addition to fluid composition and provenance studies (Kelley et
42 al., 1986; Turner & Bannon, 1992; Kendrick et al., 2001, 2006), the initial $^{40}\text{Ar}/^{36}\text{Ar}$ values of FIs in quartz can considerably
43 vary and may be used to differentiate between meteoric-sourced water (~ 298.6) (Ballentine et al., 2002; Ozima & Podosek,
44 2002) and deeper crustal or mantle-derived fluids ($>10,000$; MORB $>40,000$) (Burnard et al., 1997).
45 In order to accurately determine the age of FIs in quartz veins using the $^{40}\text{Ar}/^{39}\text{Ar}$ stepwise crushing method or the source of
46 the fluid based on $^{40}\text{Ar}/^{36}\text{Ar}$ ratios, it is necessary to consider three distinct components of ^{40}Ar , namely (1) radiogenic $^{40}\text{Ar}_{\text{R}}$
47 or $^{40}\text{Ar}^*$, which is produced in the sample itself through the radioactive decay of ^{40}K , and (2) ^{40}Ar that was initially trapped in
48 the fluid inclusion, either as (2a) atmospheric $^{40}\text{Ar}_{\text{A}}$ or (2b) excess $^{40}\text{Ar}_{\text{E}}$. The presence of $^{40}\text{Ar}_{\text{E}}$ in FIs creates a significant
49 challenge to determining accurate vein formation ages using the $^{40}\text{Ar}/^{39}\text{Ar}$ technique (Rama et al., 1965), although isochron
50 diagrams might help to overcome this issue (McKee et al., 1993; Qiu, 1996; Qiu et al., 2002). In addition to $^{40}\text{Ar}_{\text{E}}$, the origin
51 of $^{39}\text{Ar}_{\text{K}}$ (or K content) has been a topic of debate, with the possibility that the $^{39}\text{Ar}_{\text{K}}$ (and thus K) may come from the dissolved
52 salts in FIs, leaking from the crystals lattice during crushing (Kendrick et al., 2011), and/or from any K-bearing mineral
53 inclusions trapped inside the crystals (Qiu & Wijbrans, 2006; Kendrick, 2007; Qiu & Wijbrans, 2009; Kendrick & Phillips,
54 2009).
55 This study aims i) to determine the absolute age of quartz vein formation by analysing FIs using the stepwise crushing $^{40}\text{Ar}/^{39}\text{Ar}$
56 dating method, ii) to elucidate the location of K in the vein minerals (e.g., FIs, mineral inclusions, and/or crystal lattice) and
57 iii) to identify when different K sources release their $^{39}\text{Ar}_{\text{K}}$ through the examination of released argon gases during the crushing
58 process and geochemical analysis of quartz mineral samples using an Electron Probe Micro Analyser (EPMA).
59 Quartz samples were obtained from an outcrop near the Rursee in the upper reaches of the Rur river in the North Eifel region
60 of Western Germany. Detailed structural investigations of this area have been previously conducted by Van Noten et al. (2007),
61 who differentiated quartz veins into two groups. The older generation of quartz veins, the so-called bedding normal veins
62 (BNVs) is assigned to the early stages of the Variscan orogeny, whereas the second group, comprising bedding parallel veins
63 (BPVs), is linked to the main stage of the Variscan orogeny. Absolute $^{40}\text{Ar}/^{39}\text{Ar}$ ages of FIs representing the age of quartz vein



64 formation would allow us to better constrain the structural evolution and subsurface fluid flow during the Variscan orogeny in
65 north-western Europe. Reliable $^{40}\text{Ar}/^{39}\text{Ar}$ age constraints of quartz vein formation would provide the opportunity to understand
66 the timing and evolution of mountain building in analogue fold-and-thrust belts.

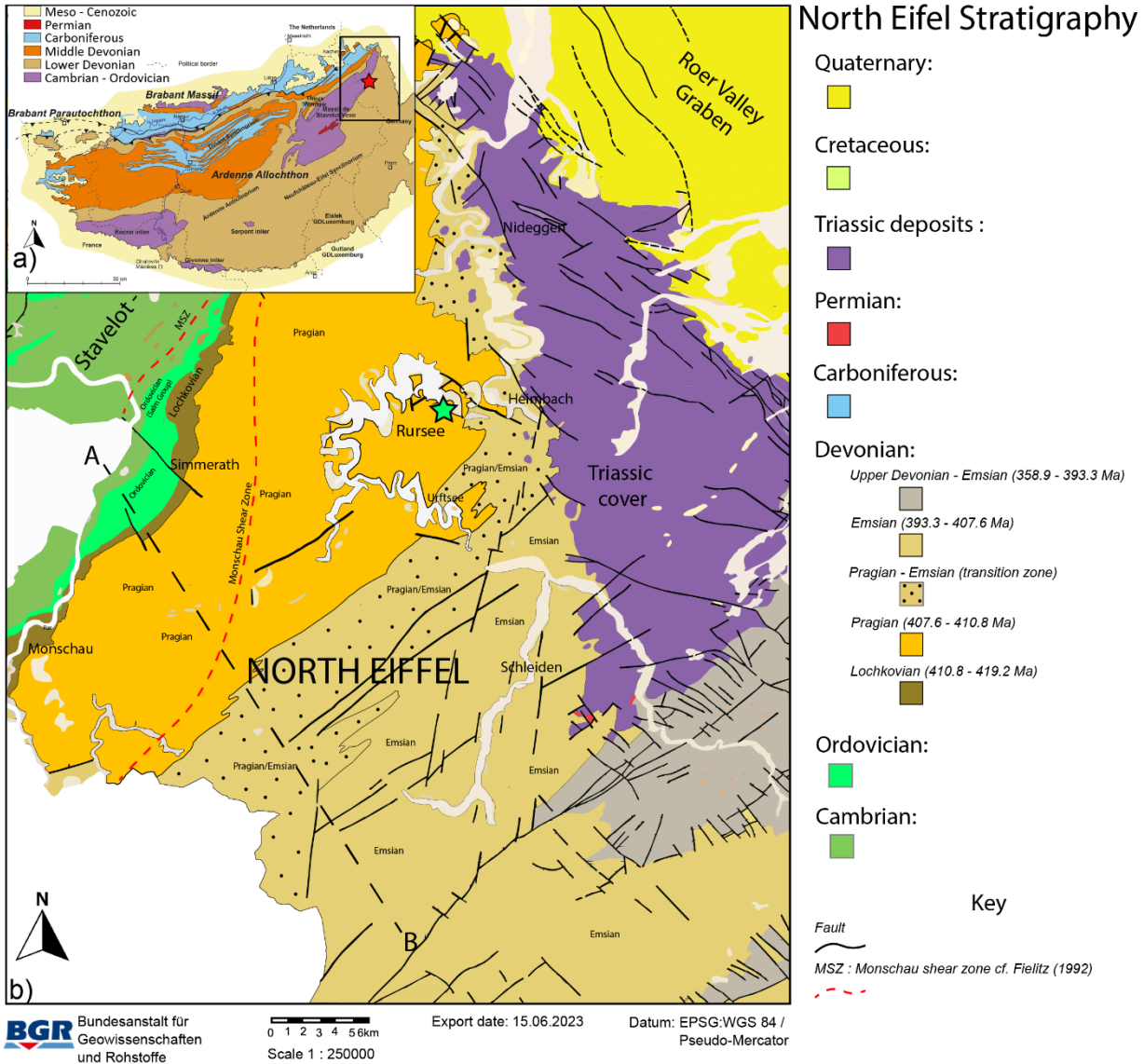
67 **1.1 Geological Setting**

68 The Rhenohercynian fold-and-thrust belt, part of the Variscan, is primarily located in the Rhenish Massif in Germany and
69 extends westward into the Ardennes, southwest England, and eastward to the Harz Mountains (Koltonik et al., 2018). The
70 Ardennes Allochthone (Fig. 1a), western part of Rhenish Massif, structurally comprises three main components: the Dinant
71 fold-and-thrust belt, the Lower Palaeozoic Inliers, and the High-Ardennes Slate Belt (HASB). The HASB primarily consists
72 of Lower Devonian metasediments including the Rurberg (upper Pragian) and Heimbach (upper Pragian to lower Emsian)
73 units.

74 For this study, quartz veins samples were collected near the Schwammenauel dam in the Rursee area of the North Eifel region,
75 Germany (Fig. 1b). The Rurberg and Heimbach units feature alternating layers of siltstones and fine- to coarse-grained
76 sandstones (Goemaere & Dejonghe, 2005), deposited in shallow marine to deltaic environments in the northern
77 Rhenohercynian Ocean (Oncken et al., 1999). The Early Devonian strata have accumulated to a total thickness of up to 7 km
78 due to rapid subsidence and deposition (Winterfeld, 1994) forming the Eifel syncline (Fig. 1b). These strata are overlain by a
79 ~3 km thick sequence of Lower Lochkovian to Pragian deposits.

80 The late Carboniferous deformation of the Variscan foreland led to initial burial metamorphism (Mansy et al., 1999), with
81 prehnite-pumpellyite facies similar to the anchizone conditions in the North Eifel area (Fielitz 1995), where temperatures
82 reached up to 220 °C (Littke et al., 2012). There is also evidence of the upward migration of warm fluids into the northern
83 Variscan front in Ardennes, driven by Variscan thrusting (Mucchez et al., 2000; Schroyen & Mucchez, 2000; Lünenschloss et
84 al., 2008).

85 Following the Variscan period, the Rhenish Massif has been affected by transpressional and transtensional deformation that
86 resulted in the formation of complex fault networks that host vein mineralization (Franzke & Anderle, 1995; Ziegler & Dèzes,
87 2005). During the Jurassic-Cretaceous period, the southern Rhenish Massif was periodically affected by hydrothermal
88 activities (Kirnbauer et al., 2012), as indicated by geochronological data for post-Variscan vein mineralization (Bonhomme et
89 al., 1983; Mertz et al., 1986; Bähr, 1987; Jakobus, 1992; Hein & Behr, 1994; Klügel, 1997; Schneider & Haack, 1997;
90 Glasmacher et al., 1998; Schneider et al., 1999; Chatziliadou & Kramm, 2009).

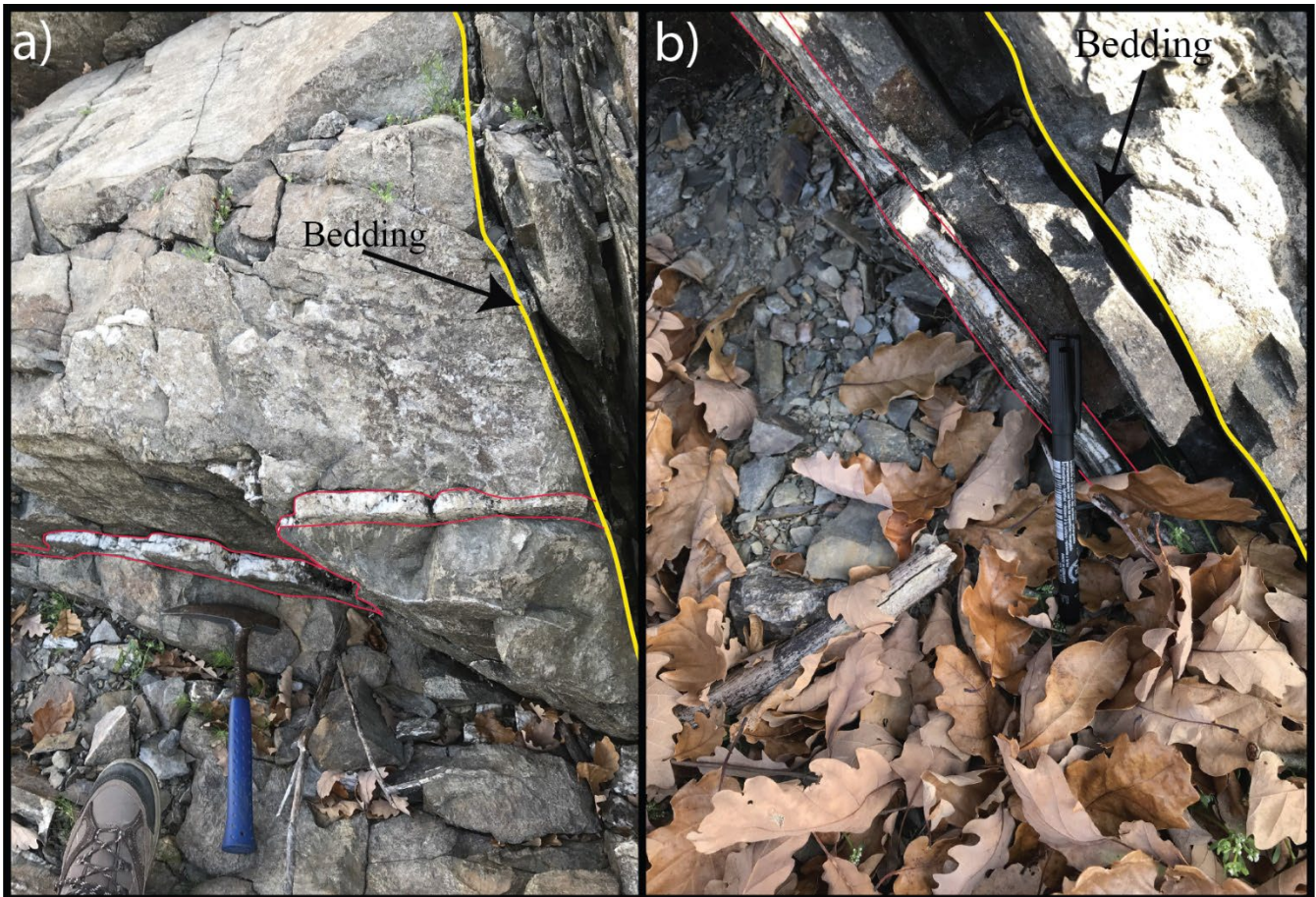


91 **Figure 1:** (a) Geological map with the Variscan frontal zone in the Ardenne-Eiffel region (study area marked with a red star).
 92 (b) Geological map of the North Eifel region (modified after Ribbert, 1992; Van Noten et al., 2011). The Lower Devonian layers overlay
 93 metamorphic deposits of the Lower Palaeozoic Stavelot-Venn Inlier. These layers have been locally distorted in the Monschau Shear
 94 Zone (MSZ), as documented by Fielitz (1992). Triassic sediments overlay the Lower Devonian layers in the eastern region. The
 95 sample location, indicated by a green star, is situated next to the Rursee reservoir, which is near the Schwammenauel dam. Below,
 96 cross-section illustrates the continuous northwest-southeast trending overturned folds that are characteristic of the North Eifel zone.



97 The $^{40}\text{Ar}/^{39}\text{Ar}$ study targets the BNVs and BPVs (Fig. 2), which formed in low-grade metamorphosed (prehnite-pumpellyite
98 facies) conditions as a result of the precipitates from warm fluids in fractures (Van Noten et al., 2008). The structural cross-
99 cutting relationships between these quartz vein generations suggest that they originated during different geological events (Van
100 Noten et al., 2008) revealing that BPVs are younger than BNVs. BNVs are found mostly within the competent psammite and
101 hardly occur in incompetent pelitic layers. This positioning suggests that BNVs formed during the early stages of the Variscan
102 orogeny, associated with the final burial phases of the Ardennes-Eifel basin (Sintubin et al., 2000; Urai et al., 2001; Van Noten
103 et al., 2008, 2009).

104 In contrast, BPVs follow the strata between the psammatic and pelitic layers as a result of the bedding-parallel slip caused by
105 flexural folding during the Variscan orogeny (Van Noten et al., 2008).



106 **Figure 2: Images of studied outcrop from the Rursee area. The image (a) presents the bedding normal veins (red lines), while (b)**
107 **shows the bedding parallel veins (red lines). Yellow lines indicate the bedding in both images.**



108 2 Material and methods

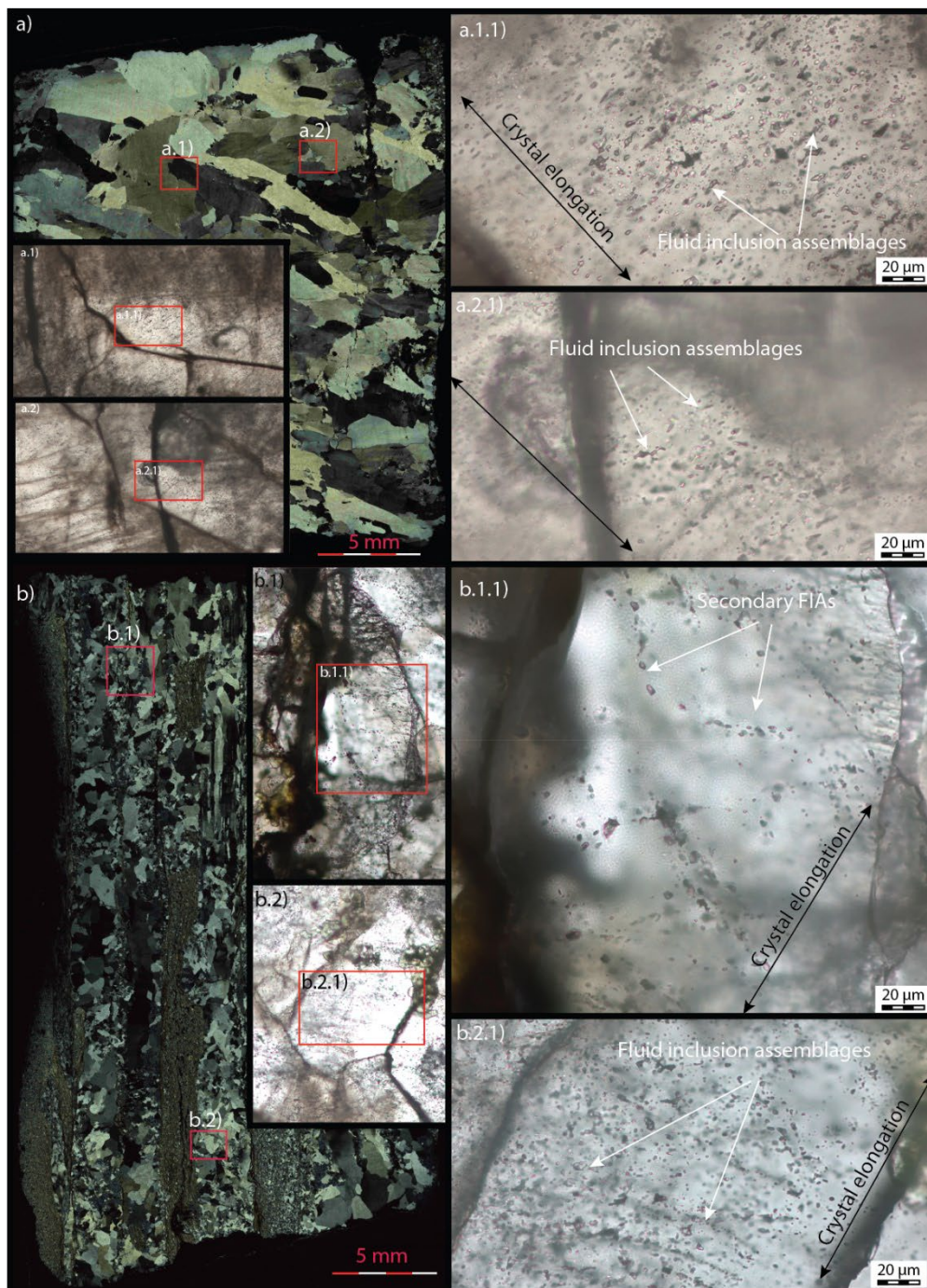
109 2.1 Quartz and inclusions in quartz minerals

110 A total of seven samples of different veins (3 BNVs and 4 BPVs) were collected from the Rursee outcrop for $^{40}\text{Ar}/^{39}\text{Ar}$ analysis
111 (Table 1). Both vein types mainly consist of elongated-fibrous milky quartz grains that are characterised by syntaxial growth,
112 whereby the growth starts from the wall of the veins towards the central part of the veins (Ramsay, 1986). The pelitic host
113 rocks consist of sericite, illite, mica and chlorite. Chlorite is also abundant within the vein fractures and between the host rock
114 and the vein wall.

115 Both quartz vein generations lack of primary FIs in the crystal growth zones and contain pseudo-secondary and secondary
116 fluid inclusion assemblages (FIAs) ($<10\ \mu\text{m}$) (Van Noten et al., 2011) in the sealed microcracks being perpendicular to crystal
117 elongation (Fig 3.). The Rursee quartz vein samples yield average FIs homogenization temperatures (minimum trapping
118 temperature, T_h) of $\sim 135 \pm 25\ ^\circ\text{C}$ and $\sim 160 \pm 20\ ^\circ\text{C}$ for BPV and BNV, respectively, with salinities of 3.5-8 eq. wt.% NaCl. In
119 general, T_h of pseudo-secondary and secondary FIs span an equally broad range of 110-180 $^\circ\text{C}$ (Van Noten et al., 2011).

120 2.2 Mineral separation

121 Prior to $^{40}\text{Ar}/^{39}\text{Ar}$ analysis, mineral separation was conducted at Vrije Universiteit Amsterdam (VU; The Netherlands). The
122 bulk vein samples were crushed, washed, and cleaned in an ultrasonic bath for at least one hour to remove the adhering host
123 rock contaminants from quartz grains. The samples were sieved into 250 and 500 μm fraction and dried in an oven at 60 $^\circ\text{C}$.
124 The samples were further separated by a custom-made system using an overflow centrifuge with conventional heavy liquids
125 based on IJlst (1973) and Frantz magnetic separation (Porat, 2006). We used heavy liquids with a density of 2.62 g/cm^3 and
126 2.64 g/cm^3 to obtain fluid inclusion-rich fraction of quartz grains ($\rho = 2.62\text{-}2.64\ \text{g}/\text{cm}^3$). The fraction was rinsed with acetone,
127 dried, and further sieved to separate the 400-500 μm grain size range. From this fraction, only the purest quartz grains were
128 hand-picked under binocular microscope for $^{40}\text{Ar}/^{39}\text{Ar}$ dating.



129 Figure 3: Fluid inclusions in quartz veins under optical microscopy. (a) Image of BNVs under cross-polarizer light microscopy. Both
130 (a.1.1) and (a.2.1) are the zoom of (a.1) and (a.2) images, respectively, indicating pseudo-secondary fluid inclusion assemblages (FIAs)
131 (white arrow). (b) Cross polarizer images of the BPV sample under microscopy. (b.1.1) and (b.2.1) images are secondary and pseudo-
132 secondary fluid inclusion (respectively) -focused areas, which are zooms of the (b.1) and (b.2) images, respectively. The white arrows
133 represent the FIAs. Both generations of quartz veins have FIAs that are present in sealed microcracks rather than in crystal growth
134 zones.



135 2.3 $^{40}\text{Ar}/^{39}\text{Ar}$ stepwise crushing

136 Fluid-rich quartz grains (400-500 μm ; 2.62-2.64 g/cm^3) were carefully selected under a binocular zoom microscope, and a
137 quantity of 200-270 mg of material was packed in aluminium foil and placed in 20 mm ID - 22mm OD aluminium cups.
138 Drachenfels (DRA-2) sanidine standard was loaded between each set of three samples to monitor the neutron flux. The samples
139 were irradiated at Oregon State University (USA) using the CLICIT (Cadmium-Lined In-Core Irradiation Tube) facility for
140 12 hours (batch VU123). After irradiation, standards were placed in 2 mm copper planchet holes for single grain fusion analysis
141 and vacuum pre-baked at 250 $^{\circ}\text{C}$. The samples were then placed in an ultra-high vacuum system, baked at 120 $^{\circ}\text{C}$, and
142 connected with hot NP10 and ST172 getters, Ti getter sponge at 400 $^{\circ}\text{C}$, and a cold trap at -70 $^{\circ}\text{C}$. The standards were fused
143 with a Synrad 48-5 CO_2 continuous-wave laser fusion system.

144 The samples were crushed in an in-house developed and built crusher consisting of a stainless-steel tube (height: 18 cm, outer
145 diameter: 1.8 cm) that has a spherical curve on its interior base and a magnetic stainless-steel pestle (height: 5 cm, diameter:
146 1.6 cm, weight: \sim 69.5 g) with rounded tips with a slightly narrower outer radius. These geometries allow optimisation of the
147 impact on the sample while crushing. Once a split of the sample (\sim 30 mg of quartz grains) was loaded into the crusher tube,
148 the pestle was carefully relocated to the bottom of the tube to avoid crushing the sample. The crush tube, the pestle, and the
149 sample were baked overnight at 250 $^{\circ}\text{C}$. The pestle was dropped into a free-fall state using an external electromagnet with a
150 frequency of 1 Hz controlled by an adjustable power supply and pulse generator to crush the sample. The pestle was dropped
151 from a height of \sim 3, \sim 4 or \sim 5 cm *in vacuo*. Subsequently, the gases emitted from FIs in the fragmented quartz sample were
152 analysed. To obtain a sufficient amount of argon in the mass spectrometer, the number of pestle drops per extraction step and
153 drop height were systematically increased during the experiment, with a maximum of 999 drops per analysis (in total, \sim 40000
154 cumulated pestle drops per experiment).

155 The gas released from the samples and standards was analysed isotopically using a ThermoFisher Scientific Helix MC+ mass
156 spectrometer. The Helix MC+ mass spectrometer is a 5 collector channel instrument, equipped with a total of 10 collectors, a
157 Faraday collector optionally fitted with a 10^{12} Ohm or 10^{13} Ohm resistor amplifier and a compact discrete dynode secondary
158 electron multiplier (CDD-SEM) collector on each collector channel. Five collectors can be used at the same time to
159 simultaneously collect the beam intensity signals of the 5 isotopes of argon. The H2-Faraday collector is employed for the
160 detection of ^{40}Ar using a 10^{13} Ohm amplifier. Similarly, the H1- CDD collector is used for the measurement of ^{39}Ar (H1
161 Faraday was used for the runs on DRA-2 sanidine standard because of the higher ^{39}Ar signal), the AX-CDD collector for ^{38}Ar ,
162 the L1-CDD collector for ^{37}Ar , and the L2-CDD collector for ^{36}Ar .

163 Line blanks were measured after every three to four unknowns and subtracted from the succeeding sample data. A Gain
164 calibration is done by correcting for gain relative to the beam intensity measured on the AX-CDD, using measurements of \sim 50
165 fA (^{40}Ar measured beam intensities) pipettes of air on each cup, and mass discrimination corrections are made by measuring a
166 series of \sim 400 fA (^{40}Ar measured beam intensities) air pipettes roughly every 12 hours. Raw data were processed using the
167 ArArCalc software (Koppers, 2002). Ages are calculated relative to Drachenfels (DRA-2) sanidine of 25.552 ± 0.078 Ma



168 (Wijbrans et al., 1995) which was recalibrated against Fish Canyon Tuff sanidine of 28.201 ± 0.023 Ma (Kuiper et al., 2008).
169 The decay constants of Min et al. (2000) are used. The atmospheric $^{40}\text{Ar}/^{36}\text{Ar}$ ratio of 298.56 ± 0.31 is based on Lee et al.
170 (2006). The correction factors for neutron interference reactions are $(2.64 \pm 0.02) \times 10^{-4}$ for $(^{36}\text{Ar}/^{37}\text{Ar})_{\text{Ca}}$, $(6.73 \pm 0.04) \times 10^{-4}$
171 for $(^{39}\text{Ar}/^{37}\text{Ar})_{\text{Ca}}$, $(1.21 \pm 0.003) \times 10^{-2}$ for $(^{38}\text{Ar}/^{39}\text{Ar})_{\text{K}}$, and $(8.6 \pm 0.7) \times 10^{-4}$ for $(^{40}\text{Ar}/^{39}\text{Ar})_{\text{K}}$. Gain correction factors and their
172 standard errors ($\pm 1\text{SE}$) are 1.00162 ± 0.00028 for H2-Far, 0.97963 ± 0.00021 for H1-CDD, 0.99921 ± 0.00027 for L1-CDD
173 and 0.96163 ± 0.00064 for L2-CDD for data measured in 2022 (R2.1) and 1.00465 ± 0.00031 for H2-Far, 0.97033 ± 0.00027
174 for H1-CDD, 0.99824 ± 0.00033 for L1-CDD, and 0.96309 ± 0.00070 for L2-CDD for data measured in 2023 (R1-R6). The
175 K/Cl ratios are calculated by $\text{K/Cl} = \beta \times ^{39}\text{Ar}/^{38}\text{Ar}$ with $\beta = 0.06$ derived from $\text{K/Cl} = \sim 18.7$ in GA1550 and $^{39}\text{Ar}_{\text{K}}/^{38}\text{Ar}_{\text{Cl}} =$
176 ~ 316 for a 12-hour irradiation at the OSU Triga CLICIT facility. All errors are quoted at the 2σ level and include all analytical
177 uncertainties (Table 1).

178 Note that it is not possible to directly correct the crushing blank because we cannot perform the exact experiment without
179 crushing sample material. We tested the blanks for each tube without sample material, following the identical procedures used
180 for real experiments. With this approach, we have direct metal-to-metal contact during pestle drops, which might not be fully
181 representative of a real sample. We did observe a substantial increase in background, with a higher number of drops and a
182 higher drop level. Importantly, the composition of this blank is similar to that of atmospheric argon. Therefore, we follow the
183 approach that the ^{40}Ar signal derived from the line blank (measured every 3-4 unknowns where we mimic the sample
184 experiment, but without the crushing / pestle drops) is subtracted from the measured ^{40}Ar intensity. The real blank has an
185 atmospheric $^{40}\text{Ar}/^{36}\text{Ar}$ ratio and is incorporated in the air corrections, leading to a lower radiogenic $^{40}\text{Ar}^*$ if the real blanks are
186 relatively high.

187 **2.4 Electron Probe Microanalysis (EPMA)**

188 Quartz grains of sub-samples that were analysed for $^{40}\text{Ar}/^{39}\text{Ar}$ were mounted in epoxy resin and carbon coated for the JEOL
189 JXA-8530F hyperprobe field emission electron probe microanalyzer (EPMA) at Utrecht Universiteit (UU; The Netherlands)
190 to define the elemental compositions of 1) the host quartz, 2) minerals that are present in FIs, filled cavities, or fractures, and
191 3) mineral inclusions in the quartz. For this analysis, an accelerating voltage of 15 kV and a beam current of 8 nA for host rock
192 (quartz) and 7 nA for mineral inclusions are used with beam sizes of $10 \mu\text{m}$ and $1 \mu\text{m}$, respectively. The elements analysed are
193 Si, Ti, Al, Fe, Mn, Ca, Na, K, P, Cl, F, Ba, and Zr. The data are calibrated using Icelandic rhyolite glass (ATHO-G) and basalt
194 glass (KL2-G) standards that were both measured with a beam size of $10 \mu\text{m}$, and multiple times before and after measurements
195 of the samples.



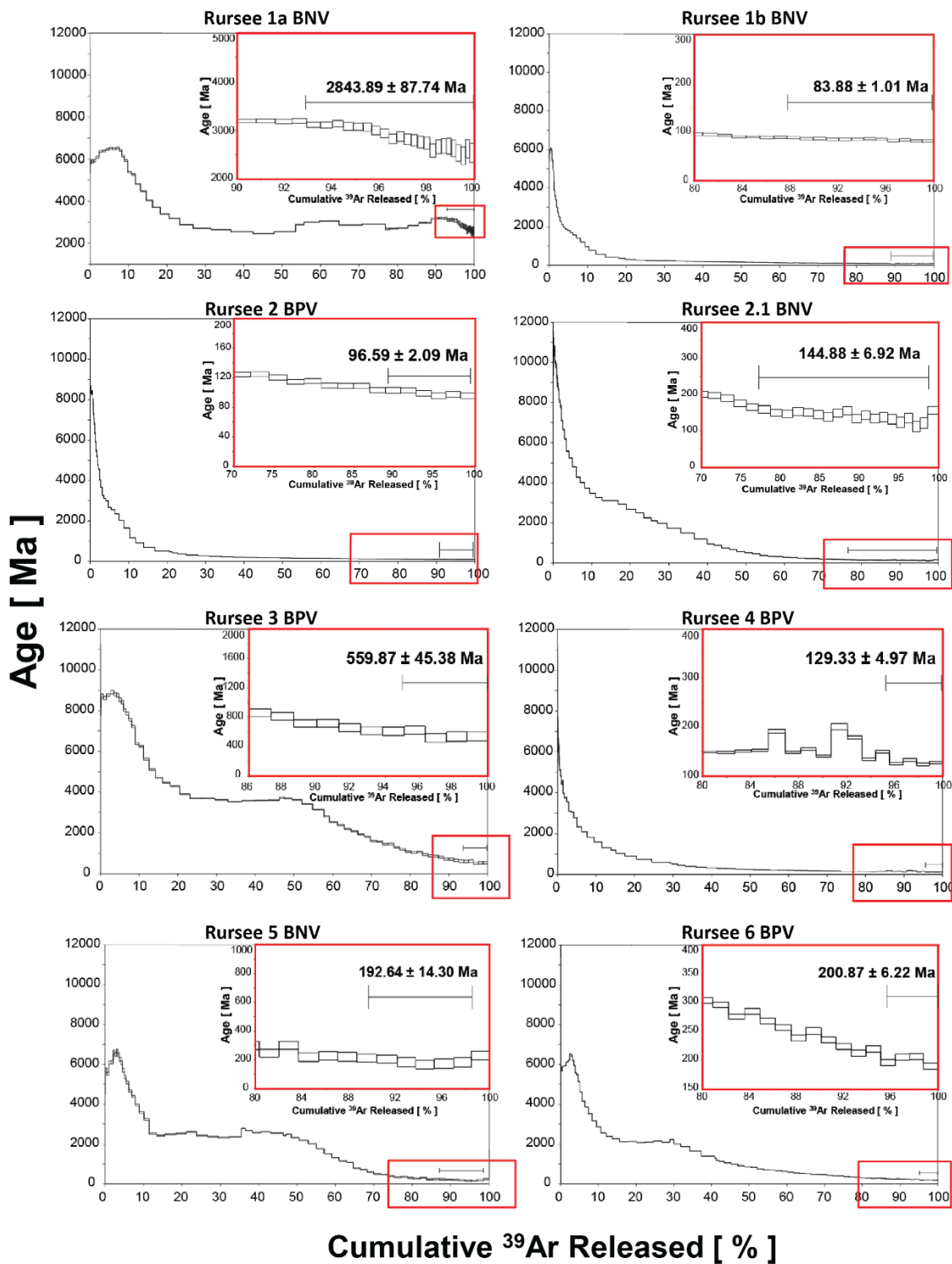
196 3 Results

197 The age spectra of the *in vacuo* stepwise crushing of the quartz samples are plotted in Figure 4. All samples show typical
198 release patterns with unrealistically old ages (>6 Ga) in the initial 10 % of $^{39}\text{Ar}_K$ released. Note that samples Rursee 1a BNV
199 and Rursee 1b BNV are measured in two different experiments on subsets from the same irradiated sample, yielding different
200 results. For sample Rursee 1a BNV, a lighter pestle (68 g) has been used than for sample Rursee 1b BNV (69.5 g) and for all
201 other samples.

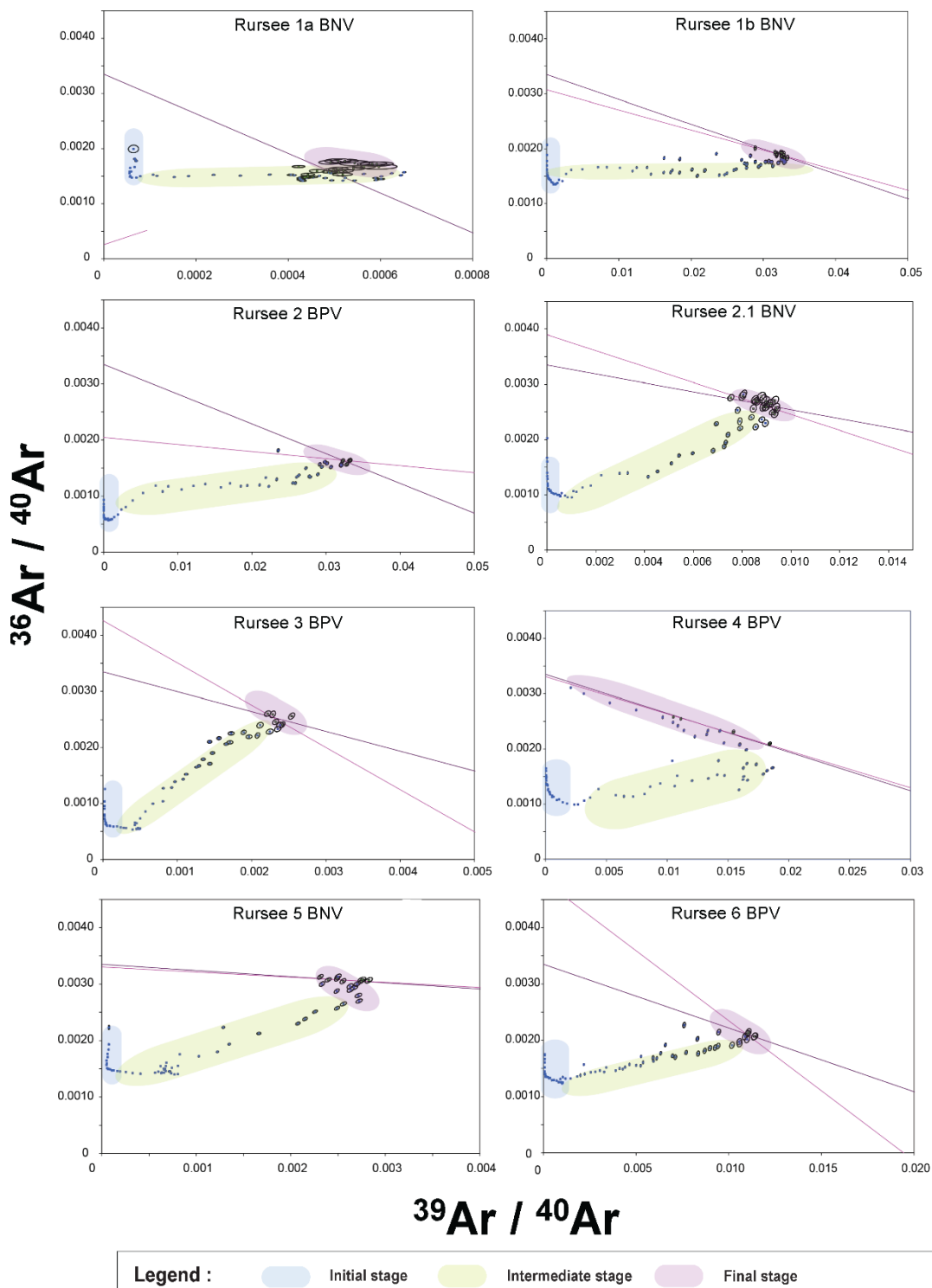
202 The apparent ages of the spectra in samples Rursee 1b BNV, Rursee 2 BPV, Rursee 2.1 BNV, and Rursee 4 BPV exhibit a
203 gradual decrease in age over the next 10 - 40 % of $^{39}\text{Ar}_K$ released, eventually stabilising at a more or less consistent age from
204 ~80 to ~100 % $^{39}\text{Ar}_K$. Rursee 3 BPV, Rursee 5 BNV, and Rursee 6 BPV show comparable behaviour with, after the initial old
205 ages, a decrease in age to a “pseudo-plateau” from ~15 % to ~40 % $^{39}\text{Ar}_K$ released, followed by a gradual decrease in age and
206 a more or less uniform age in the >80 % released $^{39}\text{Ar}_K$ part of the spectrum. For these pseudo-plateaus, we arrive at averaged
207 ages of ~84 Ma for Rursee 1b BNV, ~97 Ma for Rursee 2 BPV, ~117 Ma for Rursee 4 BPV, ~216 Ma for Rursee 2.1 BNV,
208 ~190-200 Ma for Rursee 5 BNV, and Rursee 6 BPV, and ~560 Ma for Rursee 3 BPV. The ages of Rursee 2.1 BNV and Rursee
209 4 BPV correspond to the inverse isochron ages; however, due to significant uncertainty, the ages of other samples obtained
210 from the average plateau age (Table 1).

211 The inverse isochrons (Fig. 5) confirm that the first part of all experiments is heavily affected by excess argon ($^{36}\text{Ar}/^{40}\text{Ar}$ ratios
212 are much lower than atmospheric composition), followed by an increase in $^{36}\text{Ar}/^{40}\text{Ar}$ and $^{39}\text{Ar}/^{40}\text{Ar}$ ratios and clustering of data
213 points on the reference line. The ages that we derive are based on the data points that cluster along the reference line in the
214 isochrons in the final part of the age spectra. There is no systematic age difference between BNV and BPV.

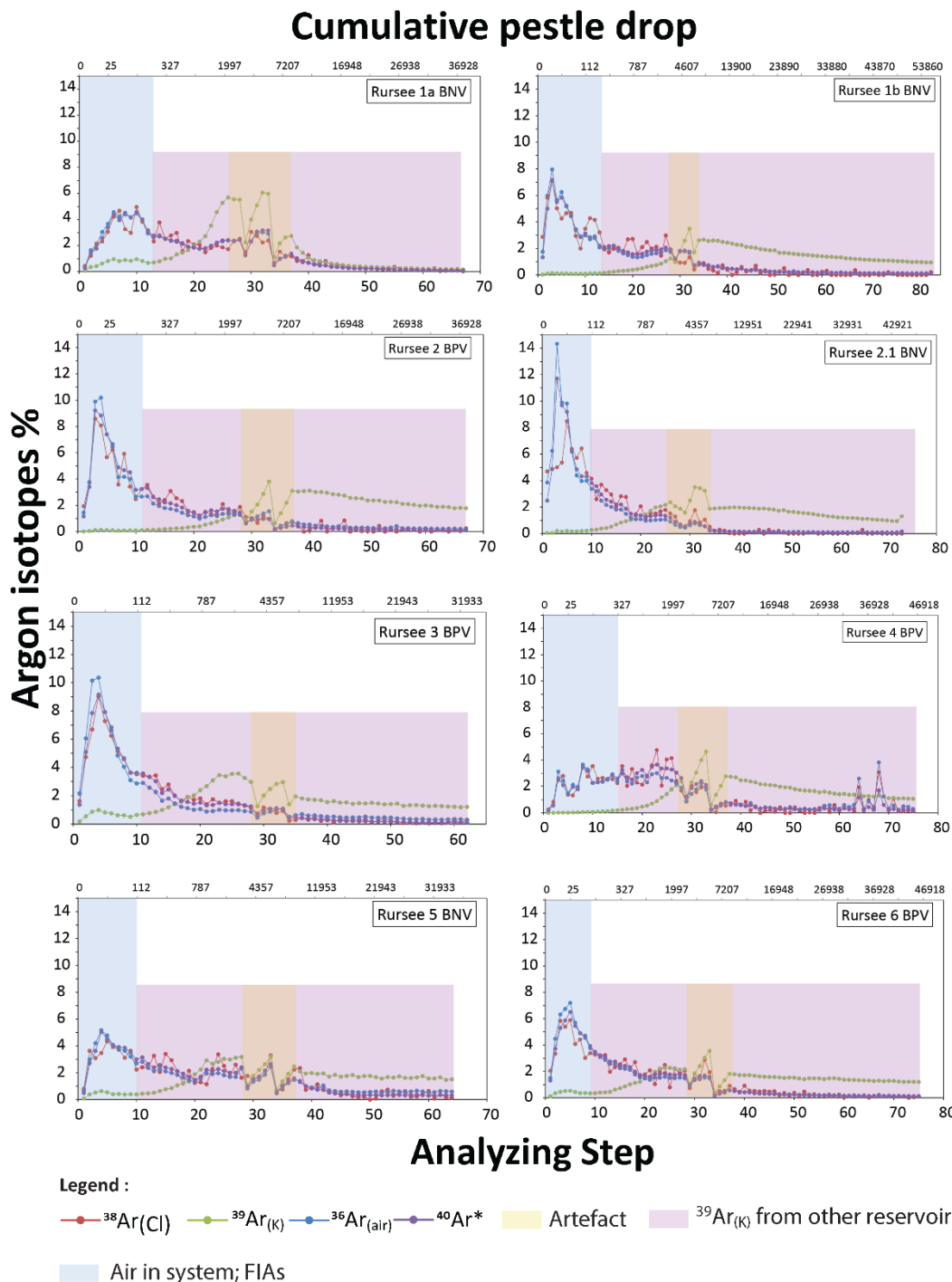
215 All quartz samples release argon during *in vacuo* stepwise crushing with different isotopes of argon contributing to the gas
216 release at different stages of the experiment. Figure 6 shows, for each step, the percentage (relative to total amount) of a specific
217 isotope that is released through the experiment. All quartz samples are characterised by a release of most of the $^{36}\text{Ar}_{\text{air}}$ in the
218 first 20 steps. $^{40}\text{Ar}^*$ and $^{38}\text{Ar}_{\text{Cl}}$ follow the pattern of $^{36}\text{Ar}_{\text{air}}$. The $^{39}\text{Ar}_K$ generally starts to increase after the first 20 analysing
219 steps (~790 pestle drops from 3 cm height). At steps 30-35, we observe fluctuations in the data. These shifts are artefacts
220 caused by increasing the drop height (from 3 to 4 cm at ~step 30 and from 4 to 5 cm at ~step 35) and adjusting the number of
221 pestle drops. To prevent high signals, we started with a relatively low number of pestle drops at a higher drop height, yielding
222 low signals, as observed as two troughs at ~step 30 and ~step 35 in all experiments. All quartz samples are low in $^{36}\text{Ar}_{\text{air}}$,
223 $^{38}\text{Ar}_{\text{Cl}}$, and $^{40}\text{Ar}^*$ at the end of analysis compared to their total release. For $^{40}\text{Ar}^*$, we still measure a small, reliable signal, but
224 this is obscured in Figure 6 due to the high signals in the first steps since we plot percentages of the total released ^{40}Ar per
225 experiment. Note that huge amounts of excess ^{40}Ar (which is part of the $^{40}\text{Ar}^*$ signal) are released in the initial steps of the
226 experiment and dominate the total percentage.



227 Figure 4: The apparent plateau age of all quartz vein experiments. The red boxes focus on the last part of the age spectra, where
 228 apparent ages are more or less stable.



229 Figure 5: Inverse isochrons of all quartz veins samples. Dark line corresponds to the atmospheric $^{36}\text{Ar}/^{40}\text{Ar}$, while pink line shows
230 mean weighted.



231 **Figure 6: Released argon isotopes per analysing step relative to its total release. Note that the data are expressed against analysing**
 232 **step instead of the crushing step, and that the upper x-axis scaling (cumulative pestle drops) are neither linear, nor logarithmic (non-**
 233 **continuous scaling).**



234 Table 1 Summary of $^{40}\text{Ar}/^{39}\text{Ar}$ age spectra, including invers isochron data of all analysed quartz samples.

| Locality | Rursee, outcrop near Schwammenauel dam (Germany) | | | | | | | |
|---|--|-------------------|--|--|---------------------------------------|--------------------------------------|--|--|
| Rock type | Quartz veins | | | | | | | |
| Mineral | Quartz | | | | | | | |
| Sample ID | Rursee 1a BNV | Rursee 1b BNV | Rursee 2 BPV | Rursee 2.1 BNV | Rursee 3 BPV | Rursee 4 BPV | Rursee 5 BNV | Rursee 6 BPV |
| Sample ID Ar | R01a | R01b | R02 | R021 | R03 | R04 | R05 | R06 |
| GPS coordinate | Lat.: 50.63378406 Long.: 6.44191402 | Long.: 6.44190753 | Lat.: 50.63377933 Long.: 6.44184657 | Lat.: 50.63388498 Long.: 6.44176707 | Lat.: 50.63418108 Long.: 6.4418217 | Lat.: 50.6344143 Long.: 6.4418217 | Lat.: 50.63367794 Long.: 6.44201891 | Lat.: 50.63392217 Long.: 6.44181953 |
| Grain Size (μm) | 400 – 500 | | | | | | | |
| Density (g.cm^{-3}) | 2.62 - 2.64 | | | | | | | |
| Age (Ma) | 2843.9 | 83.9 | 96.6 | 144.9 | 559.9 | 129.3 | 192.6 | 200.9 |
| $\pm 2\sigma$ analytical error + J error | ± 87.7 | ± 1.0 | ± 2.1 | ± 6.9 | ± 45.3 | ± 5.0 | ± 14.3 | ± 6.2 |
| $\pm 2\sigma$ full external error | ± 95.9 | ± 2.0 | ± 2.9 | ± 7.5 | ± 46.5 | ± 5.6 | ± 14.8 | ± 7.4 |
| MSWD | 42.8 | 1.6 | 3.34 | 4.34 | 6.05 | 5.39 | 2.01 | 0.37 |
| K/Ca | 0.32 | 1.54 | 14.28 | 5.33 | 0.285 | 3.21 | 0.75 | 3.48 |
| $^{40}\text{Ar}/^{36}\text{Ar}$ inverse isochrone intercept | 3874 | 326 | 858 | 258 | 329 | 311 | 289 | 243 |
| $\pm 2\sigma$ analytical error + J error | ± 7284.5 | ± 51.1 | ± 860.2 | ± 38.4 | ± 183.4 | ± 6.4 | ± 29.0 | ± 180.8 |
| Inverse isochrone age | - | 74.1 | 80.7 | 215.5 | 399.2 | 116.7 | 258.6 | 26.2 |
| $\pm 2\sigma$ analytical error + J error | ± 5769.6 | ± 16.0 | ± 224.8 | ± 50.6 | ± 425.1 | ± 7.1 | ± 129.0 | ± 176.5 |
| $\pm 2\sigma$ full external error | ± 5769.7 | ± 16.0 | ± 224.8 | ± 50.8 | ± 425.2 | ± 7.5 | ± 129.1 | ± 176.6 |
| n/n_{tot} (n: number of analyses included, weighted mean, n_{tot} : total number of analysis) | 22 / 67 | 11 / 83 | 4 / 67 | 19 / 73 | 4 / 62 | 4 / 75 | 9 / 64 | 3 / 75 |
| MSWD | 14.48 | 1.56 | 0.19 | 3.82 | 8.83 | 0.87 | 2.21 | 0.46 |



235 4 Discussion

236 During *in vacuo* stepwise crushing, the release of argon isotopes from the samples follows systematic patterns. The challenge
237 is to link this release of argon from the samples to the different potential reservoirs of K and, as a next step, the geological
238 meaning of the age and elemental ratios of K/Cl and Ca/Cl. Here, we first discuss potential issues related to the analytical
239 quality of the data. Next, we discuss potential reservoirs of K and subsequently $^{40}\text{Ar}^*$ to link these options to our results, and
240 to finally assess the ages and their broader implications.

241 4.1 Data quality

242 4.1.1 Rursee 1a/1b BNV

243 We speculate that for the experiment Rursee 1a BNV, we sampled a smaller part of the argon reservoirs in the quartz minerals
244 comparable to the first 10 % of the spectrum of Rursee 1b BNV. This is corroborated by the fact that for Rursee 1a BNV, 46
245 mg of quartz released 12.7 fA $^{39}\text{Ar}_K$ (0.3 fA/mg quartz), while for Rursee 1b BNV, 89.1 fA was released from 25 mg of quartz
246 (3.6 fA/mg of quartz). We therefore do not further discuss the results of Rursee 1a BNV, but note that sample heterogeneity
247 might also have contributed to this difference.

248 4.1.2 Impact of blank correction

249 Blank correction procedure likely does not impact weighted mean age computation; however, it does influence the $^{40}\text{Ar}/^{36}\text{Ar}$
250 intercept of the inverse isochron. This is only the case when the regression line has a non-radiogenic intercept that is different
251 from the atmospheric $^{36}\text{Ar}/^{40}\text{Ar}$. When the intercept is within the error overlapping with the atmospheric ratio, the blank
252 correction only causes the point to move along the regression line as comes out of the discussion below as well. We described
253 our blank correction procedure in methods (see supplementary file 1). The fact that we cannot mimic the dropping of the pestle
254 when a sample is present in the tube provides limitations on how well we can determine the blank during the experiments. The
255 blank tends to increase with higher number of pestle drops, but composition of this blank is atmospheric. For the test of the
256 blank, we used quartz glass fragments to mimic zero-age minerals, as a blank determination using metal on metal impacts was
257 considered to be an unrealistic scenario. As a next test we artificially increase the ^{40}Ar blank (and thus the ^{36}Ar blank) assuming
258 atmospheric composition. If the data are located on the mixing line between radiogenic and atmospheric argon, this should not
259 affect isochron age (pink part – final stage in fig. 5 or 11). We tested this for sample Rursee 1b BNV with an age of ~88 Ma.
260 The $^{40}\text{Ar}/^{36}\text{Ar}$ intercepts increase with increasing blank values, and the weighted mean plateau ages change with a maximum
261 of 2.5 Ma in the chosen example. We therefore conclude that the isotopic ages remain largely unaffected, by varying the
262 amounts of atmospheric argon of the blanks. Note, that if the isochron is not a mixing line between radiogenic and atmospheric
263 argon (e.g. blue and green parts in fig 5 or 11), this assumption is incorrect. The $^{40}\text{Ar}/^{36}\text{Ar}$ intercept is then pulled away from
264 the real $^{40}\text{Ar}/^{36}\text{Ar}$ composition in the direction of the atmospheric $^{40}\text{Ar}/^{36}\text{Ar}$ intercept. Consequently, in the intercept with the
265 inverse isochrons' X-axis (and thus age) will also be affected.



266 4.1.3 Recoil artefacts

267 These artefacts occur when ^{37}Ar and ^{39}Ar , which are formed from K and Ca isotopes, form with kinetic energy. As a result,
268 they can travel from their original sites to other sites, potentially even into the adjacent phase (Turner & Cadogan, 1974;
269 Foland, 1983; Lo & Onstott, 1989; Féraud & Courtillot, 1994; Baksi, 1994; Onstott et al., 1995; Villa, 1997). However, this
270 phenomenon is assumed to have a smaller impact than that of the blank correction.

271 4.2 Potential reservoirs of K

272 To date, three main hypotheses are being debated as to the origin of the released argon in a stepwise crushing experiment. The
273 first group (Qiu & Wijbrans, 2006, 2008; Bai et al., 2019) suggests that progressive crushing releases gases mainly from FIs
274 and therefore represents FIs ages. The second group (e.g., Kendrick and Philips (2007)) discusses the possibility of K-bearing
275 mineral inclusions within the inclusion cavity and/or in microcracks serving as argon reservoirs in the later stages of crushing.
276 Obtained ages therefore represent mineral closure ages or a mixture of FIs and mineral ages.

277 In addition, the third potential source of potassium in the quartz minerals might be the presence of minor amounts of K^+ in the
278 crystal lattice (Kendrick et al., 2011) of quartz minerals, which is representative of the formation age of veins. Hydrothermal
279 quartz veins, characterised by their substitution in crystal structure, have been studied by Weil (1984) and Götze et al. (2021).
280 These studies indicate that Si^{4+} derived from hydrothermal quartz veins has the ability to be substituted by other ions such as
281 Al^{3+} , Ga^{3+} , Fe^{3+} , B^{3+} , Ge^{4+} , Ti^{4+} , and P^{4+} . Al^{3+} is most commonly replacing Si^{4+} since it is found in significant quantities (~300-
282 700 ppm) in quartz, based on EPMA data. Additionally, small quantities of monovalent ions such as K^+ may fill empty spaces
283 in the crystal structure, serving as charge balancers for trivalent substitutional ions such as Al^{3+} (Bambauer, 1961; Kats, 1962;
284 Perny et al., 1992; Stalder et al., 2017; Potrafke et al., 2019). However, Jourdan et al. (2009) postulated that the substitution of
285 these components may be so minor that it is even undetectable using a Secondary Ion Mass Spectrometer (SIMS). Furthermore,
286 it is important to note that not all hydrothermal sources or quartz minerals have this particular form of substitution (Jourdan et
287 al., 2009).

288 Apart from these potential $^{39}\text{Ar}_{\text{K}}$ reservoirs above, detrital minerals (e.g., mica present in the surrounding pelitic rock) that
289 might be trapped by the quartz veins during the growth may also contribute to the obtained ages.

290 4.2.1 Identification of different K reservoirs in the Rursee quartz samples

291 During *in vacuo* stepwise crushing, the release of argon isotopes from the samples follows systematic patterns. Here, we
292 attempt to link this release to the sequential contributions of different reservoirs of K and, thus, argon from the Rursee samples.
293 The release patterns of $^{36}\text{Ar}_{\text{air}}$, $^{38}\text{Ar}_{\text{Cl}}$, $^{39}\text{Ar}_{\text{K}}$, and $^{40}\text{Ar}^*$ (Fig. 6) for all quartz vein samples may originate from multiple existing
294 argon reservoirs.

295 Depending on the size (<10 μm), location, and generation of FIs, they may contribute successively to the argon release patterns
296 in the early or middle stage of stepwise crushing. Figure 6 reveals that the concentration of $^{39}\text{Ar}_{\text{K}}$ increases throughout the



297 process of *in vacuo* stepwise crushing, while the concentration of other argon isotopes decreases. This suggests that K-
298 containing reservoirs were not opened in the first part of the experiment. The release patterns of $^{39}\text{Ar}_K$ can be categorised into
299 two distinct groups during stepwise crushing:

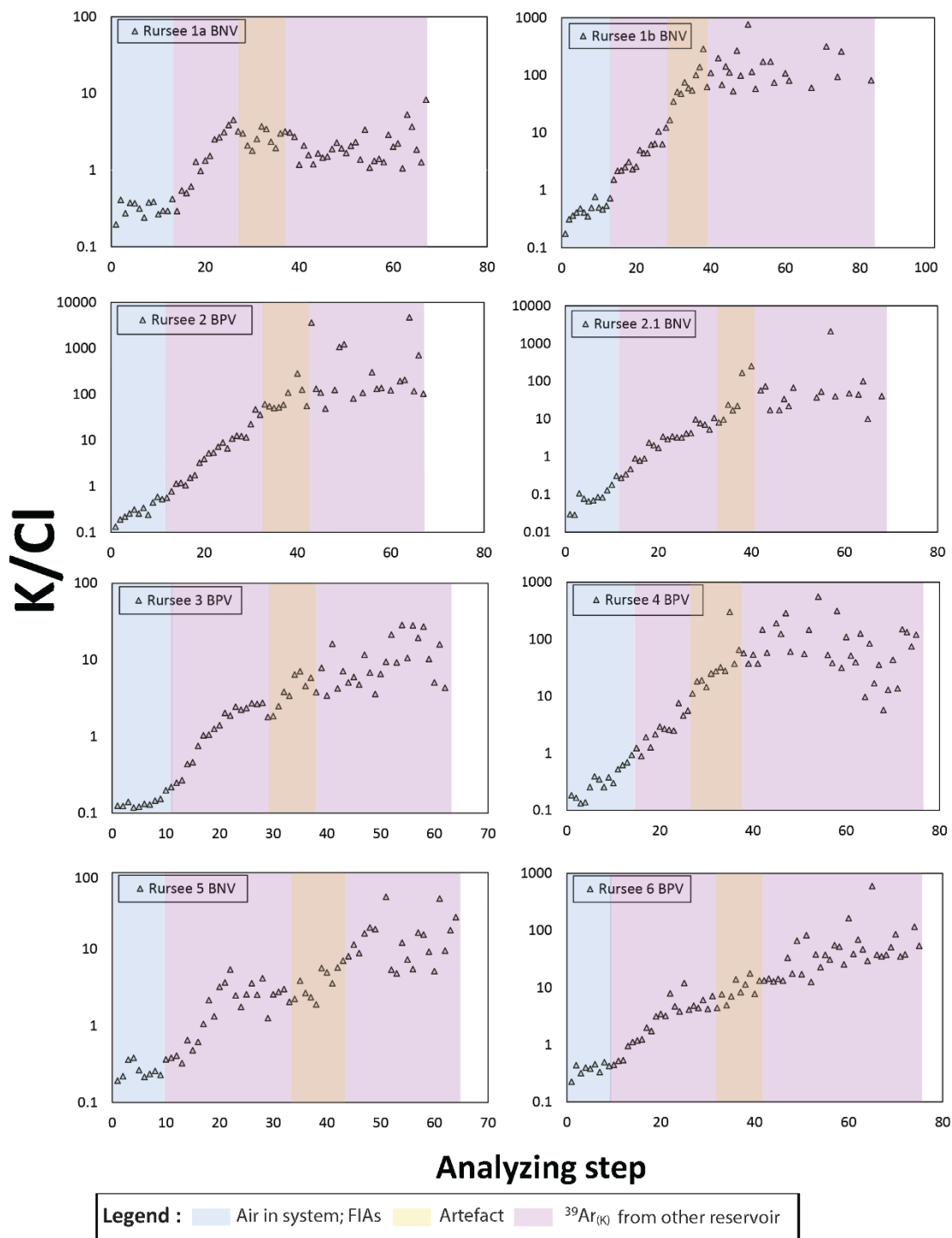
- 300 a) The *first group* of samples exhibits a small initial release during the early stages, followed by a decrease in the $\sim 10^{\text{th}}$
301 step and an increase from the $\sim 10^{\text{th}}$ to $\sim 35^{\text{th}}$ step followed by a gradual decrease (Rursee 3 BPV, Rursee 5 BNV, and
302 Rursee 6 BPV).
- 303 b) The *second group*, on the other hand, lacks the initial release of $^{39}\text{Ar}_K$ steps 1-10, but behaves the same for step 10
304 onwards with a gradual increase to the $\sim 35^{\text{th}}$ step followed by a gradual decrease (Rursee 1b BNV, Rursee 2 BPV,
305 Rursee 2.1 BNV, and Rursee 4 BPV).

306 The continuous rise in $^{39}\text{Ar}_K$ levels after ~ 10 steps in both sample groups, suggests that the gas release process can be divided
307 into at least two phases. Initially, during the first ~ 10 steps, $^{39}\text{Ar}_K$ is emitted from FIs in microcracks (secondary FIs). From
308 steps $\sim 10^{\text{th}}$ to $\sim 70^{\text{th}}$, the release occurs as a result of mixing of potential pseudo-secondary FIs (~ 10 - $\sim 15^{\text{th}}$ steps), mineral
309 inclusions and/or the crystal lattice of quartz veins. This interpretation is supported by the K/Cl correlation plots (Fig. 7), which
310 show a consistent lower K/Cl ratio until the $\sim 10^{\text{th}}$ step.

311 From the 10^{th} to the 15^{th} K/Cl ratio, it reaches ~ 1 with a steep rise for all quartz samples, and later (from $\sim 20^{\text{th}}$ step) this ratio
312 continues to increase steeply for *the second group* of samples, while it shows a less pronounced increase for *the first group* of
313 samples.

314 The lower K/Cl ratio may be attributed to the presence of Cl and a lack of or limited amounts of K in combination with
315 relatively constant low salinity levels (3.5-8 eq. wt.% NaCl) inside the FIs, which are likely to be opened in the early phase.
316 After most FIs have been mechanically opened, the subsequent rapid increase in K (reflected by the $^{39}\text{Ar}_K$) and the steady
317 decline in Cl (reflected by the $^{38}\text{Ar}_{Cl}$) occur throughout successive crushing steps and is reflected in the K/Cl ratio. Therefore,
318 this increase is most likely caused by the exhaustion of the Cl-rich FIs in combination with the presence of minerals containing
319 potassium and/or potassium from the crystal lattice of quartz that release their argon in the later crushing steps.

320 This approach to distinguish between FIs and other K reservoirs was first suggested by (Kendrick et al., 2006, 2011): K/Cl
321 ratios ≤ 1 are representative for FIs and K/Cl ratios > 1 for other sources. Therefore, if K/Cl ≤ 1 , the obtained age corresponds
322 to the age of the FIs. If the K/Cl > 1 the obtained age corresponds to the age of the trapped K-bearing mineral and/or K from
323 the crystal lattice (Kendrick et al., 2006, 2011). In our samples the K/Cl is greater than 1 after the first $\sim 15 \pm 3$ steps in all quartz
324 vein samples, indicating the presence of major K-related reservoir(s) other than FIs. It is worth noting that this is based on the
325 assumption that there are no other K-bearing phases, such as KNO_3 , K_2SO_4 or K_2CO_3 , rather than KCl dissolved in aqueous
326 FIs. This assumption seems to be verified by Raman analysis (see Figure A1), which does not show detectable peaks for these
327 alternative K-bearing phases. Therefore, K/Cl > 1 suggests that K does not only relate to the salinity of the FIs, and at least one
328 major other source should be present, e.g., the crystal lattice of quartz and/or mineral inclusions in the quartz crystals and/or
329 in microcracks.



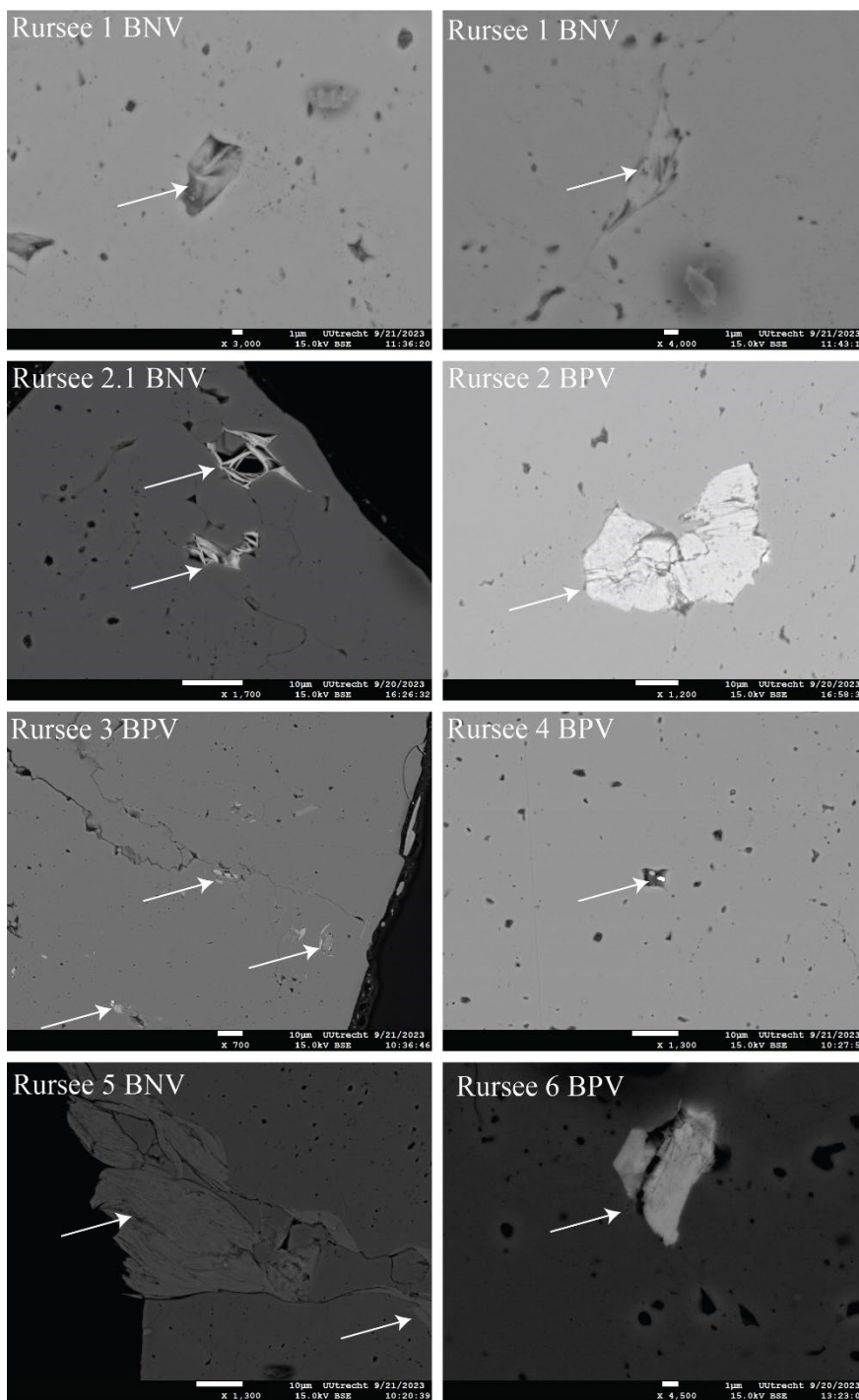
330 Figure 7: K/Cl ratios plotted against analyzing steps for all quartz veins.



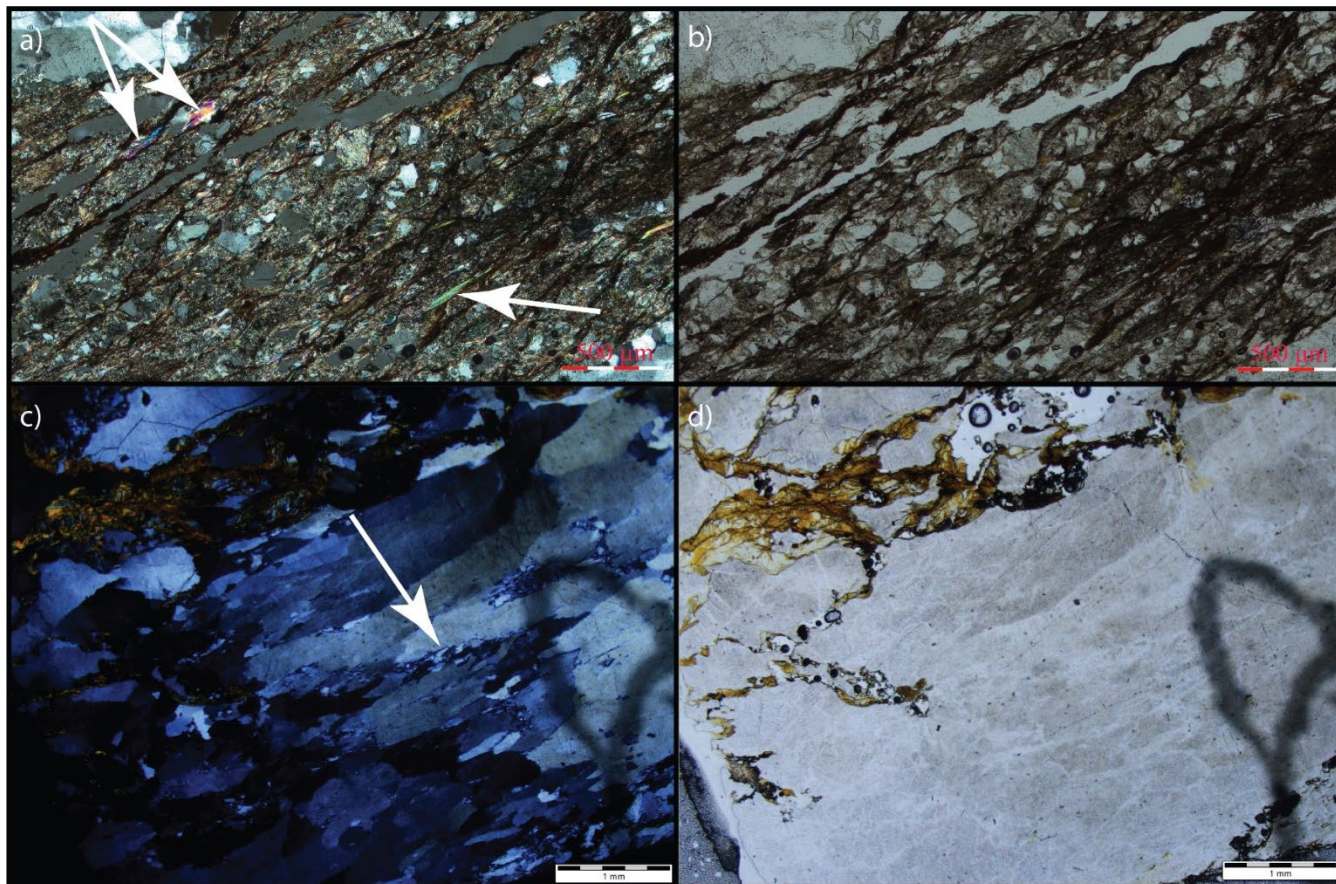
331 4.2.2 K-bearing mineral inclusions

332 EPMA data (Table 2) from cleaned hand-picked fluid-rich separated quartz grains indicate the presence of sericite, chlorite-
333 sericite and illite-sericite in the microfractures and in the cavities of fluid inclusion, which might explain the subsequent
334 increase of $^{39}\text{Ar}_K$ from the $\sim 10^{\text{th}}$ analysing step onwards. The presence of these minerals (or mixtures) in the inclusion cavity
335 and microfractures is also invisible under a binocular or petrographic microscope during the mineral separation, but it was also
336 captured using electron-backscattered imaging (Fig. 8). In thin sections of quartz veins with associated host rock, illite-sericite
337 and white mica are abundant in the surrounding pelitic layer of the Rursee formation (Fig. 9). These minerals that contain a
338 significant amount of K_2O are also detected by EPMA, in the separated quartz samples, especially in Rursee 2 BPV (see EPMA
339 data, Table 2). High K concentrations (~ 8.8 wt. % K_2O) are likely related to intergrowth with sericite or a closely-related
340 mineral.

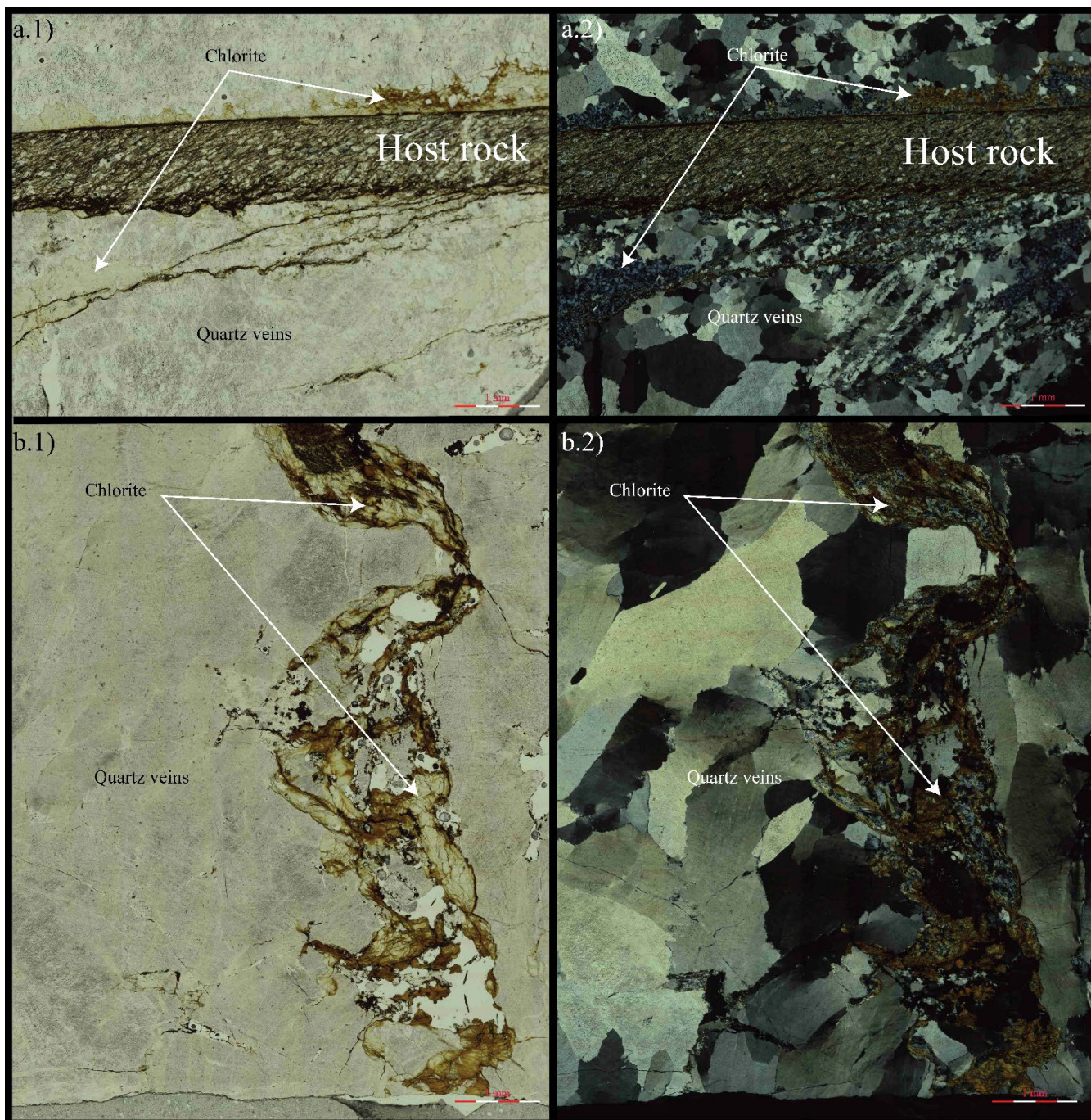
341 Additionally, petrographic analysis of thin sections of whole rock samples representing both vein generations (BPV and BNV)
342 show an abundance of chlorite in between the vein wall and host rock, as well as in fractures (Fig. 10). Despite the absence of
343 K in the crystal structure of chlorite, traces of K were reported for chlorites in previous studies (Pacey et al., 2020; Li et al.,
344 2022).



345 Figure 8: Images of mineral inclusions under electron-backscattered SEM. Secondary minerals (e.g. chlorite, sericite and mica)
346 occur in cavities and microfractures (pointed by white arrow) in separated fluid-rich quartz fraction as determined using EPMA.



347 **Figure 9: Microscopic image of the quartz veins host rock matrix from the Rursee formation. (a) Cross polarizer (b) plane polarizer**
348 **images of the pelitic host rock (Rursee 2 BPV). White arrows (image a) indicate the presence of the mica and sericite in the host**
349 **pelitic rock. (c) Cross polarizer (d) plane polarizer images of the quartz veins matrix (Rursee 1 BNV). White arrow (image c) shows**
350 **the presence of the quartz sub-grains. The presence of quartz sub-grains in the veins are due to the local tectonic activity, indicating**
351 **that this period is correspond to tectonic activity.**



352 Figure 10: Chloritization distribution in the vein wall and in fractures for both generations of quartz veins. (a) Plane (a.1) and cross
353 (a.2) polarizer of bedding parallel veins: chloritization mainly between vein wall and host rock, and fractures. (b) Plane (b.1) and
354 cross (b.2) polarizer of bedding normal veins: chloritization in fractures.



355 4.2.3 K from crystal lattice and detrital minerals

356 EPMA analyses of quartz matrix indicate that K concentrations in the crystal lattice are below the detection limit of ~100 ppm.
357 A maximum K concentration of ~100 ppm K (for example, 100 ppm K in Rursee 2.1 BNV) and an age of 144 Ma would result
358 in ~16000 fA $^{40}\text{Ar}^*$ when measured on our Helix-MC mass spectrometer, which is a comparable amount of total $^{40}\text{Ar}^*$ released
359 from K-bearing mineral inclusion. Given the large amount of sample (~30 mg), this would translate into a significant
360 contribution of K from the crystal lattice of quartz. We therefore suggest that K in the crystal lattice may contribute to the
361 observed $^{40}\text{Ar}^*$ signals (see calculation on supplementary file 2).

362 In this study, argon molecules might also be derived from secondary minerals in cracks as well as embedded detrital minerals
363 (e.g., mica from host rock). This interpretation aligns with the observation that the homogenization temperatures of FIs within
364 the quartz veins are below the closure temperature for argon in detrital minerals. Under such conditions, the expected ages
365 from K-bearing detrital minerals would correspond to pre-Variscan periods, reflecting the age of the deposits hosting the quartz
366 veins, while the obtained ages are significantly younger in this study. Therefore, we infer that detrital minerals do not
367 significantly contribute to the $^{40}\text{Ar}^*$ signals.

368 To summarise, during the first stages (until the ~20th analysis steps) of the stepwise *vacuo* crushing, gases are likely released
369 only from FIs (secondary and pseudo-secondary, as is also observed for FI in garnets (Qiu & Wijbrans, 2006, 2008)). Huseynov
370 et al. (2024) demonstrated that a significant amount of fluid inclusion water can be extracted from these samples by a single
371 crushing step using a spindle crusher. In this study, throughout the crushing process, the total amount of argon released steadily
372 increases (Fig. 6). In the latter stages of the experiment (from the 20th analysing steps), the substantial release of $^{39}\text{Ar}_K$ isotopes
373 may support the hypothesis proposed by Kendrick and Philips (2007) and Kendrick et al., (2011), suggesting the presence of
374 K-bearing mineral inclusions in the samples and/or $^{40}\text{Ar}^*$ from the crystal lattice and also non-crushed small-sized FIs (<5 μm).
375 The presence of K-bearing mineral inclusions is also corroborated by EPMA data, and the presence of K in the lattice cannot
376 be ruled out for the Rursee samples.

377 4.3 Age spectra and isochrons

378 As aforementioned, the distribution of argon isotopes (Fig. 6) indicates that $^{39}\text{Ar}_K$ is derived from distinct sources, likely
379 mineral inclusions and/or eventually crystal lattice rather than FIs in particular in the later phase of the experiment, which was
380 used for the age determinations. These various sources of K, including fluid and mineral inclusions and/or crystal lattice, may
381 all contribute to the variability observed in the age spectra derived from the different samples. Due to the presence of $^{40}\text{Ar}_E$
382 from the FIs, the initial analytical stages of the analyses yield anomalously high ages in the first part of their age spectra (Fig.
383 4). Some samples (Rursee 3 BPV, Rursee 5 BNV, and Rursee 6 BPV) show a "pseudo-plateau" in the first part of the
384 experiment. The "pseudo-plateau" effect occurs between the 20-30th analysing steps, which may be associated with sudden
385 changes in K/Cl ratios (Fig. 7). These sudden changes may be due to sharp transition from fluids states reservoirs (e.g. small
386 sized FIs) to solid states reservoirs (e.g. K-bearing mineral inclusions). However, it does not occur in *the second group* quartz

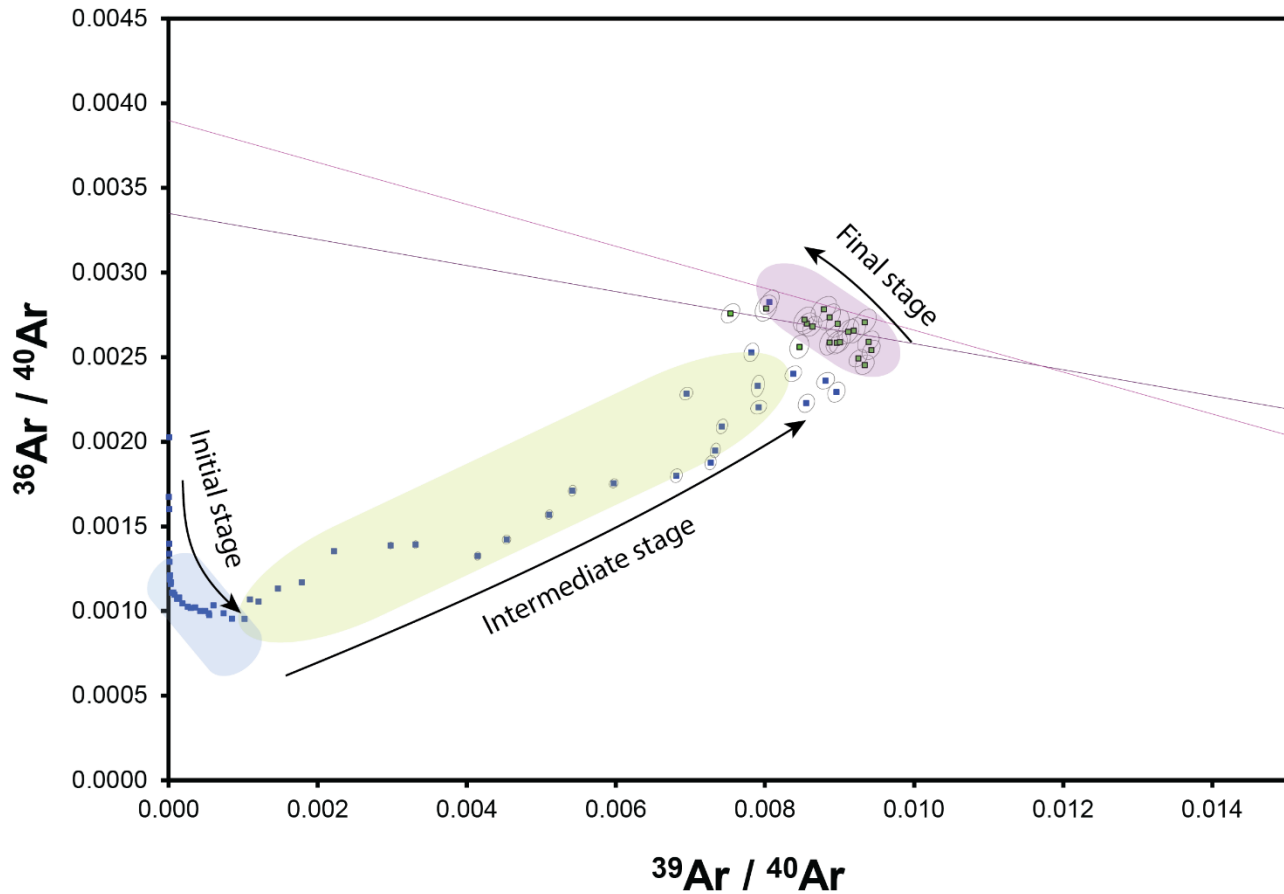


387 samples (Rursee 1b BNV, Rursee 2 BPV, Rursee 4 BPV) revealing smooth transitions from fluids to solid states $^{39}\text{Ar}_K$
388 reservoirs. The transition for the Rursee 2.1 BNV is neither abrupt like for the *first group* samples nor smooth as for the *second*
389 *group* samples; hence, the impact of the “pseudo-plateau” is minimal.

390 The transition from fluid state reservoirs to solid state reservoirs can be supported by grain size distribution (see supplementary
391 file 4), indicating that fluid state reservoirs may remain unreleased beyond around 800 crushes (around the 20th analysis step).
392 However, the accumulation of small particles at the bottom of the crusher (non-recoverable size) after 800 crushes, may result
393 in the measured results not accurately representing the whole grain size distribution. As the grain size distribution depends on
394 many factors (i.e., crushing efficiency, presence of microcracks), even for separated clean quartz grains, that may be a factor
395 of difference for two groups.

396 The impact of $^{40}\text{Ar}_E$ results in inverse isochrons (Fig. 5) during the initial stage. The relationship between the $^{36}\text{Ar}/^{40}\text{Ar}$ and
397 $^{39}\text{Ar}/^{40}\text{Ar}$ for all samples resulted in a decrease in the $^{36}\text{Ar}/^{40}\text{Ar}$ ratio and an increase in the $^{39}\text{Ar}/^{40}\text{Ar}$ ratio (initial stage in Fig.
398 11). The presence of an elevated concentration of ^{36}Ar at the beginning of the experiment could be either due to the atmospheric
399 argon gas that is trapped in the stainless steel crusher and/or the original fragment surfaces and perhaps released during the
400 initial stage of crushing. Following the opening of FIs, the ratio of $^{36}\text{Ar}/^{40}\text{Ar}$ increases linearly with the ratio of $^{39}\text{Ar}/^{40}\text{Ar}$. This
401 is probably due to a decrease in excess argon throughout the crushing and an increase in $^{39}\text{Ar}_K$ associated with K-bearing
402 minerals and/or crystal lattice (intermediate stage in Fig. 11). In the last phase of $^{40}\text{Ar}/^{39}\text{Ar}$ analysis, the concentration of $^{39}\text{Ar}_K$
403 decreases (final stage in Fig. 11). This last part is particularly important for determining the age of quartz vein samples.

404 Inverse isochrons may assist in determining the age of FIs by linear regression of the data related to FIs. However, the high
405 amounts of excess argon in the system obscure geologically meaningful ages.



406 **Figure 11: Inverse isochron representation of quartz veins (ex: Rursee 2.1 BNV): 3 stages: (1) initial stage with opening of fluid**
407 **inclusions; (2) intermediate stage where argon is released from mineral inclusions or microfractures and/or crystal lattice; (3) Final**
408 **stage of argon release from mineral inclusions and neglectable excess argon in samples.**



409 4.4 Implications

410 Unlike studies that obtained consistent ages from FIs (Qiu & Wijbrans, 2006; Qiu et al., 2011; Bai et al., 2013, 2019), we were
411 unable to date FIs in Rursee quartz samples, likely due to high $^{40}\text{Ar}_\text{E}$ concentrations and/or low salinity. While no age was
412 determined for the FIs, $^{40}\text{Ar}/^{36}\text{Ar}$ ratios (above atmospheric but below 4000) indicate a mixed metamorphic-meteoritic fluid
413 source (Ballentine et al., 2002; Ozima & Podosek, 2002). Later, during the crushing experiment, the K-bearing mineral
414 inclusions may provide geologically meaningful ages although the argon closure temperatures in quartz remain uncertain. For
415 reference, the closure temperature of smaller size sericite grains ($\sim 20\ \mu\text{m}$) correspond to temperatures ($\sim 300\text{-}350\ \text{°C}$)
416 (Glasmacher et al., 2001; Watson & Cherniak, 2003), while the vitrinite reflectance from psammatic and pelitic layers indicate
417 maximum burial temperatures ($220\ \text{°C}$) near the Carboniferous-Permian boundary, with gradual cooling thereafter (Littke et
418 al., 2012).

419 The obtained $^{40}\text{Ar}/^{39}\text{Ar}$ ages (117-84 Ma) differ from the interpretation based on structural analyses, which posit that veining
420 occurred during the early Variscan Orogeny (Van Noten et al., 2007), possibly due to argon loss during cooling and/or
421 recrystallization. The obtained ages may be influenced to some extent by the presence of neo-crystallized quartz sub-grains,
422 although their volume appears relatively small (Fig. 9c). However, since the ages primarily reflect solid-phase reservoirs (i.e.,
423 K-bearing mineral inclusions) rather than fluid-phase components, it is likely that K-bearing solid-phase reservoirs intergrowth
424 simultaneously with the recrystallization process.

425 Post-Variscan tectonic activity is known for southern Rhenish Massif due to late- and post-orogenic fault movements and
426 coeval reactivation of Variscan structures leading to the fluids (re)activity (Herbst & Muller, 1969; Schwab, 1987; Korsch &
427 Schäfer, 1991; Hein & Behr, 1994; Moe, 2000; Kirnbauer et al., 2012).

428 Given that reactivation of existing veins could have occurred without forming new fractures (Virgo et al., 2013), this
429 reactivation is usually associated with the infiltration of high saline ($>20\ \text{eq. wt.}\% \text{ NaCl}$) fluids in Central Europe and the
430 Rhenish Massif (Behr et al., 1987; Redecke, 1992; Hein & Behr, 1994; Germann & Friedrich, 1999; Heijlen et al., 2001;
431 Kučera et al., 2010).

432 This saline fluid activity is at odds with the low-salinity FIs ($3.5\text{-}8\ \text{eq. wt.}\% \text{ NaCl}$) in the Rursee quartz veins (Van Noten et
433 al., 2011). However they agree with low saline FIs in quartz veins of the Rhenish Massif, which are attributed to upward
434 migration of Variscan fluid remnants during Jurassic-Cretaceous reactivation (Kirnbauer et al., 2012).

435 Near Rursee (Stavelot Inlier), low saline ($0.2\text{-}7.2\ \text{eq. wt.}\% \text{ NaCl}$) and high-temperature fluid activity ($\sim 250\ \text{°C}$) along the
436 Variscan front reflect warm meteoritic fluid circulation (Schroyen & Muechez, 2000). Such warm, low saline fluids may have
437 also contributed to chloritization of veins in the in Rursee outcrops. We propose that tectonic activity and quartz vein
438 reactivation could possibly explain the observed $^{40}\text{Ar}/^{39}\text{Ar}$ ages, as low saline Variscan fluids perhaps moved along the
439 reactivated fractures, forming new quartz minerals within the Variscan-related veins during Jurassic-Cretaceous tectonic
440 activity (i.e. opening of North Atlantic).



441 **Table 2 Elemental analysis of quartz grain, microcracks, and mineral inclusions in quartz vein samples under EPMA.**

EPMA analysis of mineral inclusions and microfractures of clean fraction of quartz veins grain of Rursee samples (wt.%).

| | Sample ID | Grain ID | SiO ₂ | TiO ₂ | Al ₂ O ₃ | FeO | MnO | MgO | CaO | Na ₂ O | K ₂ O | P ₂ O ₅ | Cl | F | BaO | ZrO ₂ | O | H ₂ O | TOTAL |
|-------------------------|--------------|----------|------------------|------------------|--------------------------------|-------|------|-------|-------|-------------------|------------------|-------------------------------|------|------|------|------------------|--------|------------------|--------|
| Internal standard of UU | KL2-1 | | 51.90 | 2.56 | 13.50 | 10.74 | 0.17 | 7.47 | 10.74 | 2.39 | 0.48 | 0.23 | bdl | bdl | bdl | bdl | 0.00 | 0.00 | 100.01 |
| | | | 51.20 | 2.51 | 13.36 | 10.79 | 0.17 | 7.46 | 10.83 | 2.38 | 0.47 | 0.27 | 0.00 | bdl | bdl | bdl | 0.00 | 0.00 | 99.28 |
| | | | 50.80 | 2.55 | 13.41 | 10.98 | 0.16 | 7.31 | 10.96 | 2.34 | 0.51 | 0.26 | 0.00 | bdl | bdl | 0.00 | 0.00 | 0.00 | 99.13 |
| Internal standard of UU | ATHO-1 | | 75.73 | 0.21 | 12.23 | 3.28 | 0.11 | 0.11 | 1.67 | 3.85 | 2.73 | 0.02 | 0.05 | 0.06 | 0.09 | bdl | 0.00 | 0.00 | 100.10 |
| | | | 75.61 | 0.24 | 12.44 | 3.47 | 0.12 | 0.13 | 1.63 | 3.73 | 2.78 | 0.05 | 0.05 | 0.03 | 0.00 | 0.02 | 0.00 | 0.00 | 100.29 |
| | | | 75.69 | 0.28 | 12.30 | 3.43 | 0.12 | 0.11 | 1.60 | 3.78 | 2.81 | 0.02 | 0.03 | 0.04 | 0.04 | 0.10 | 0.00 | 0.00 | 100.35 |
| Rursee quartz veins | Rursee 1 BNV | B_1.01a | 99.75 | 0.02 | 0.00 | 0.00 | 0.00 | bdl | 0.01 | 0.02 | 1.00 | 0.01 | 0.59 | bdl | bdl | bdl | 0.00 | 0.00 | 101.21 |
| | | B_1.02a | 55.07 | bdl | 0.31 | 0.29 | 0.01 | 0.61 | 0.88 | 0.39 | 0.51 | 0.13 | 0.40 | bdl | 0.03 | 0.01 | 0.00 | 0.00 | 58.57 |
| | | B_1.03a | 71.35 | 0.02 | 0.69 | 2.83 | 0.07 | 14.04 | 0.15 | 0.38 | 0.51 | 0.05 | 0.12 | bdl | bdl | 0.00 | 0.00 | 0.00 | 90.05 |
| | | B_1.03b | 38.76 | 0.04 | 2.80 | 1.85 | 0.02 | 6.30 | 0.74 | 1.53 | 0.95 | 0.13 | 0.30 | bdl | 0.04 | bdl | 0.00 | 0.00 | 53.29 |
| | | B_1.06a | 47.68 | 0.01 | 37.73 | 0.04 | bdl | 0.04 | 0.19 | 5.61 | 0.86 | 0.05 | 0.06 | 0.04 | bdl | bdl | 0.00 | 0.00 | 92.27 |
| | | B_1.06b | 99.52 | bdl | 0.67 | 0.01 | 0.01 | 0.00 | 0.05 | 0.04 | 0.04 | 0.05 | 0.00 | 0.00 | 0.02 | 0.05 | 0.00 | 0.00 | 100.45 |
| | | B_1.06c | 92.43 | 0.02 | 5.79 | bdl | bdl | 0.04 | 0.05 | 1.01 | 0.28 | 0.01 | 0.03 | bdl | 0.05 | bdl | 0.00 | 0.00 | 99.60 |
| | | B_1.06d | 50.05 | 0.03 | 25.07 | 0.01 | 0.02 | 0.10 | 0.08 | 2.44 | 3.24 | 0.05 | 0.03 | 0.02 | 0.00 | bdl | 0.00 | 0.00 | 81.10 |
| | | B_1.10a | 50.90 | 0.03 | 33.68 | 0.13 | bdl | 0.13 | 0.05 | 1.66 | 6.22 | 0.00 | 0.12 | 0.04 | 0.04 | bdl | 0.00 | 0.00 | 92.98 |
| | B_1.11a | 52.33 | bdl | 31.93 | 0.09 | 0.00 | 0.08 | 0.07 | 0.29 | 8.08 | 0.07 | 0.03 | 0.02 | 0.15 | bdl | 0.00 | 0.00 | 93.00 | |
| | B_1.15a | 68.06 | 0.02 | 24.01 | 0.00 | 0.00 | 0.10 | 0.39 | 3.14 | 0.93 | bdl | 0.13 | bdl | 0.03 | 0.03 | 0.00 | 0.00 | 96.82 | |
| | Rursee 2 BPV | B_2.02a | 78.24 | bdl | 0.25 | 0.32 | 0.00 | 0.04 | 0.37 | 0.22 | 0.03 | 0.19 | 0.05 | bdl | 0.05 | 0.03 | 0.00 | 0.00 | 79.76 |
| | | B_2.02b | 13.65 | 0.03 | 1.51 | 59.78 | bdl | 0.31 | 0.37 | 1.52 | 0.95 | 0.16 | 0.61 | 0.02 | bdl | 0.04 | 0.00 | 0.00 | 78.90 |
| | | B_2.03a | 47.72 | 0.07 | 6.23 | 5.85 | 0.15 | 5.35 | 3.09 | 1.64 | 0.40 | 0.05 | 0.20 | 0.04 | bdl | 0.01 | 0.00 | 0.00 | 70.79 |
| | | B_2.03b | 55.38 | 0.58 | 2.11 | 12.35 | 0.34 | 9.12 | 12.46 | 0.64 | 0.24 | 0.02 | 0.07 | bdl | 0.04 | bdl | 0.00 | 0.00 | 93.29 |
| B_2.03c | | 35.63 | bdl | 0.79 | 37.24 | 0.15 | 0.22 | 1.06 | 1.02 | 0.56 | 0.12 | 0.25 | 0.00 | bdl | 0.01 | 0.00 | 0.00 | 77.02 | |
| B_2.04a | | 24.10 | 0.01 | 22.59 | 30.81 | 0.18 | 7.20 | 0.03 | 0.04 | 0.03 | 0.05 | 0.01 | 0.00 | 0.03 | 0.01 | 0.00 | 0.00 | 85.09 | |
| B_2.05a | 24.15 | 0.04 | 22.79 | 31.10 | 0.15 | 8.04 | bdl | 0.01 | bdl | 0.00 | 0.00 | bdl | bdl | bdl | 0.00 | 0.00 | 86.14 | | |
| B_2.09a | 23.19 | 0.04 | 23.09 | 33.29 | 0.20 | 7.22 | 0.03 | 0.01 | 0.03 | 0.00 | 0.02 | 0.02 | 0.00 | 0.01 | 0.00 | 11.05 | 98.18 | | |
| B_2.09b | 47.70 | 0.05 | 35.29 | 0.83 | 0.02 | 0.88 | 0.01 | 0.28 | 8.78 | 0.00 | 0.02 | 0.13 | 0.13 | bdl | 0.00 | 4.59 | 98.70 | | |
| B_2.12a | 100.15 | bdl | 0.06 | 1.62 | 0.00 | 0.01 | 0.02 | 0.01 | 0.00 | 0.06 | 0.02 | bdl | bdl | bdl | 0.00 | 0.00 | 101.78 | | |
| B_2.12b | 56.62 | bdl | 1.83 | 26.39 | 0.02 | 0.04 | 0.05 | 0.13 | 0.33 | 0.55 | 0.32 | 0.07 | 0.00 | 0.00 | 0.00 | 0.00 | 86.34 | | |

442



443 **Table 2 (continue).**

| | Sample ID | Grain ID | SiO ₂ | TiO ₂ | Al ₂ O ₃ | FeO | MnO | MgO | CaO | Na ₂ O | K ₂ O | P ₂ O ₅ | Cl | F | BaO | ZrO ₂ | O | H ₂ O | TOTAL | |
|---------------------|----------------|-----------|------------------|------------------|--------------------------------|-------|-------|------|------|-------------------|------------------|-------------------------------|------|------|------|------------------|------|------------------|--------|--------|
| Rursee quartz veins | Rursee 2.1 BNV | B_2.1-03 | 97.91 | 0.02 | 0.04 | 1.69 | 0.00 | 0.01 | 0.00 | 0.01 | 0.00 | 0.00 | 0.02 | bdl | 0.00 | bdl | 0.00 | 0.00 | 99.58 | |
| | | B_2.1-05a | 100.31 | bdl | 0.32 | 0.19 | 0.02 | 0.02 | 0.00 | 0.02 | 0.01 | 0.00 | bdl | bdl | bdl | bdl | bdl | 0.00 | 0.00 | 100.80 |
| | | B_2.1-07a | 45.73 | bdl | 0.36 | 0.11 | 29.58 | 0.22 | 1.79 | 0.38 | 1.25 | 0.02 | 0.29 | bdl | bdl | bdl | bdl | 0.00 | 0.00 | 77.74 |
| | | B_2.1-07b | 52.22 | 0.02 | 0.24 | 0.05 | 24.09 | 0.21 | 1.52 | 0.29 | 0.89 | 0.00 | 0.22 | bdl | bdl | 0.03 | bdl | 0.00 | 0.00 | 78.46 |
| | | B_2.1-07c | 61.70 | 0.01 | 0.23 | 0.10 | 21.09 | 0.20 | 1.21 | 0.18 | 0.72 | 0.01 | 0.25 | bdl | bdl | 0.02 | bdl | 0.00 | 0.00 | 84.39 |
| | | B_2.1-11a | 40.79 | 0.07 | 26.15 | 19.64 | 0.10 | 3.03 | 0.01 | 0.28 | 3.65 | 0.03 | 0.03 | 0.03 | 0.05 | 0.12 | 0.05 | 0.00 | 0.00 | 94.03 |
| | | B_2.1-11b | 67.46 | 0.01 | 15.25 | 4.91 | 0.01 | 0.84 | 0.07 | 0.14 | 3.41 | 2.12 | 0.03 | 0.13 | bdl | bdl | bdl | 0.00 | 0.00 | 94.24 |
| | Rursee 3 BPV | B_3.02a | 42.77 | 0.01 | 15.84 | 22.60 | 0.17 | 4.89 | 0.07 | 0.02 | 0.67 | 0.07 | 0.15 | bdl | bdl | bdl | bdl | 0.00 | 0.00 | 87.12 |
| | | B_3.02b | 66.75 | 0.02 | 9.82 | 13.59 | 0.08 | 3.14 | bdl | 0.05 | 0.17 | 0.02 | 0.03 | 0.00 | 0.04 | 0.02 | 0.00 | 0.00 | 0.00 | 93.70 |
| | | B_3.02c | 90.77 | 0.02 | 3.20 | 3.97 | 0.03 | 1.03 | bdl | bdl | 0.04 | 0.01 | 0.00 | 0.00 | 0.00 | 0.05 | 0.00 | 0.00 | 0.00 | 99.08 |
| | | B_3.02d | 24.66 | 0.01 | 21.55 | 27.73 | 0.16 | 6.22 | 0.06 | 0.04 | 0.79 | 0.53 | 0.21 | 0.07 | bdl | 0.00 | 0.00 | 0.00 | 0.00 | 81.96 |
| B_3.05a | | 30.48 | 0.03 | 23.88 | 25.27 | 0.16 | 7.25 | 0.03 | 0.03 | 0.29 | 0.04 | 0.06 | bdl | bdl | bdl | bdl | 0.00 | 0.00 | 87.44 | |
| B_3.05b | | 39.46 | 0.00 | 30.20 | 13.10 | 0.06 | 2.88 | 0.05 | 0.16 | 2.88 | 0.18 | 0.10 | 0.08 | bdl | 0.09 | 0.00 | 0.00 | 0.00 | 89.24 | |
| B_3.05c | | 64.23 | 0.03 | 16.31 | 2.75 | 0.00 | 1.11 | 0.01 | 0.11 | 4.01 | 0.01 | 0.06 | bdl | bdl | bdl | bdl | 0.00 | 0.00 | 88.58 | |
| B_3.08a | | 56.03 | 0.26 | 21.87 | 6.45 | 0.01 | 2.10 | 0.02 | 0.15 | 4.74 | 0.03 | 0.00 | 0.09 | 0.05 | bdl | 0.00 | 0.00 | 0.00 | 91.79 | |
| B_3.08b | | 70.37 | 0.01 | 10.47 | 12.40 | 0.05 | 2.86 | 0.03 | 0.00 | 0.62 | 0.01 | 0.02 | 0.00 | 0.03 | bdl | 0.00 | 0.00 | 0.00 | 96.82 | |
| B_3.08c | | 71.23 | bdl | 15.55 | 3.49 | 0.03 | 0.74 | 0.04 | 7.15 | 0.08 | bdl | 0.01 | 0.01 | bdl | bdl | bdl | 0.00 | 0.00 | 98.29 | |
| B_3.08d | 32.87 | 0.73 | 19.01 | 25.07 | 0.13 | 8.40 | 0.01 | 0.07 | 0.09 | 0.01 | 0.01 | bdl | bdl | 0.01 | 0.00 | 0.00 | 0.00 | 86.40 | | |
| Rursee 4 BPV | B_3.11a | 64.26 | 0.01 | 1.66 | 9.68 | 0.06 | 0.00 | 0.23 | 0.33 | 0.13 | 0.17 | 0.16 | 0.02 | 0.03 | bdl | 0.00 | 0.00 | 0.00 | 76.76 | |
| | B_3.11b | 51.24 | bdl | 12.87 | 20.70 | 0.11 | 4.48 | 0.01 | bdl | 0.01 | bdl | 0.01 | 0.02 | 0.03 | 0.05 | 0.00 | 0.00 | 0.00 | 89.48 | |
| | B_4.02a | 47.91 | 0.07 | 3.98 | 1.07 | 0.01 | 0.22 | 0.58 | 2.30 | 2.47 | 0.15 | 0.34 | 0.10 | 0.06 | bdl | 0.00 | 0.00 | 0.00 | 59.23 | |
| | B_4.03 | 100.84 | 0.00 | bdl | 0.02 | 0.00 | 0.00 | 0.02 | 0.00 | 0.02 | bdl | 0.02 | bdl | 0.08 | bdl | 0.00 | 0.00 | 0.00 | 100.78 | |
| | B_4.04 | 32.13 | 0.05 | 3.95 | 22.69 | 0.00 | 0.15 | 6.00 | 0.63 | 0.64 | 0.17 | 0.27 | 0.13 | bdl | 0.01 | 0.00 | 0.00 | 0.00 | 66.80 | |
| | B_4.05 | 85.80 | 0.00 | 0.03 | 0.01 | 0.02 | 0.02 | 0.32 | 0.02 | 0.03 | 0.24 | 0.03 | bdl | 0.71 | bdl | 0.00 | 0.00 | 0.00 | 87.15 | |
| | B_4.08 | 78.34 | 0.01 | 0.73 | 0.04 | 10.49 | 0.22 | 0.96 | 0.07 | 0.09 | 0.00 | 0.06 | bdl | bdl | bdl | bdl | 0.00 | 0.00 | 90.27 | |
| | Rursee 5 BNV | B_5-03 | 60.18 | 0.12 | 1.28 | 1.08 | 0.05 | 1.33 | 3.01 | 0.98 | 0.97 | 0.11 | 0.37 | 0.00 | bdl | bdl | 0.00 | 0.00 | 0.00 | 69.38 |
| | | B_5-05 | 96.03 | 0.12 | 0.42 | 0.22 | 0.03 | 0.02 | 0.08 | 0.07 | 0.11 | 0.04 | 0.01 | bdl | 0.00 | 0.00 | 0.00 | 0.00 | 0.00 | 97.09 |
| | | B_5-06a | 39.40 | 0.03 | 5.43 | 49.86 | 0.21 | 0.23 | 0.17 | 0.27 | 0.51 | 0.93 | 0.19 | 0.00 | bdl | 0.07 | 0.00 | 0.00 | 0.00 | 97.27 |
| B_5-06b | | 48.32 | 0.09 | 36.38 | 0.65 | 0.00 | 0.66 | 0.03 | 0.45 | 9.16 | 0.01 | 0.01 | 0.10 | 0.15 | bdl | 0.00 | 0.00 | 0.00 | 95.97 | |
| B_5-06c | | 47.07 | 0.05 | 34.95 | 0.69 | bdl | 0.67 | 0.06 | 0.35 | 9.02 | 0.00 | 0.02 | 0.14 | 0.06 | 0.06 | 0.00 | 0.00 | 0.00 | 93.12 | |
| | B_5-07 | 83.67 | 0.01 | 8.19 | 0.07 | bdl | 0.03 | 0.13 | 0.09 | 2.24 | 0.07 | 0.03 | bdl | bdl | 0.00 | 0.00 | 0.00 | 0.00 | 94.48 | |



445 Table 2 (continue).

| | Sample ID | Grain ID | SiO ₂ | TiO ₂ | Al ₂ O ₃ | FeO | MnO | MgO | CaO | Na ₂ O | K ₂ O | P ₂ O ₅ | Cl | F | BaO | ZrO ₂ | O | H ₂ O | TOTAL |
|-------------------------|--------------|----------|------------------|------------------|--------------------------------|-------|------|------|-------|-------------------|------------------|-------------------------------|------|------|------|------------------|------|------------------|--------|
| Rursee quartz veins | Rursee 6 BPV | B_6-07b | 85.19 | 0.02 | 8.13 | 0.00 | bdl | bdl | 0.12 | 1.28 | 0.71 | 0.07 | 0.03 | bdl | bdl | 0.02 | 0.00 | 0.00 | 95.52 |
| | | B_6-07a | 79.39 | 0.00 | 3.32 | 0.00 | 0.01 | 0.03 | 0.31 | 0.06 | 0.94 | 0.24 | 0.09 | bdl | bdl | bdl | 0.00 | 0.00 | 84.32 |
| | | B_6-16a | 49.44 | bdl | 37.34 | 0.06 | bdl | 0.10 | 0.08 | 5.13 | 1.63 | 0.01 | 0.02 | 0.05 | 0.04 | bdl | 0.00 | 0.00 | 93.85 |
| | | B_6-16b | 57.16 | 0.01 | 19.71 | 0.03 | bdl | 0.06 | 0.16 | 2.85 | 1.57 | 0.03 | 0.03 | bdl | 0.05 | bdl | 0.00 | 0.00 | 81.61 |
| | | B_6-17 | 30.47 | 0.03 | 21.91 | 31.64 | 0.17 | 6.42 | 0.01 | 0.02 | bdl | 0.02 | 0.02 | bdl | bdl | bdl | 0.00 | 0.00 | 90.55 |
| Internal standard of UU | KL2-2 | B_6-19 | 69.23 | 0.04 | 17.80 | 0.12 | bdl | 0.04 | 0.46 | 4.81 | 0.00 | 0.03 | 0.00 | 0.01 | bdl | 0.00 | 0.00 | 92.51 | |
| | | | 50.09 | 2.55 | 13.10 | 10.78 | 0.17 | 6.99 | 10.80 | 2.33 | 0.47 | 0.25 | 0.00 | 0.00 | 0.01 | bdl | 0.00 | 0.00 | 97.49 |
| | | | 50.37 | 2.59 | 13.11 | 10.79 | 0.14 | 6.93 | 10.94 | 2.42 | 0.51 | 0.25 | 0.00 | bdl | 0.04 | bdl | 0.00 | 0.00 | 98.00 |
| Internal standard of UU | ATHO-2 | | 50.27 | 2.65 | 13.13 | 10.83 | 0.16 | 6.97 | 10.93 | 2.30 | 0.46 | 0.27 | 0.01 | bdl | bdl | 0.01 | 0.00 | 0.00 | 97.95 |
| | | | 74.10 | 0.23 | 12.11 | 3.37 | 0.10 | 0.11 | 1.63 | 3.60 | 2.80 | 0.03 | 0.05 | 0.04 | 0.04 | 0.02 | 0.00 | 0.00 | 98.23 |
| | | | 74.00 | 0.24 | 12.22 | 3.38 | 0.10 | 0.09 | 1.59 | 3.60 | 2.68 | 0.03 | 0.04 | 0.10 | 0.06 | 0.01 | 0.00 | 0.00 | 98.13 |
| Internal standard of UU | KL2-3 | | 74.39 | 0.21 | 12.11 | 3.41 | 0.10 | 0.09 | 1.63 | 3.55 | 2.70 | 0.06 | 0.04 | 0.02 | 0.08 | 0.08 | 0.00 | 0.00 | 98.48 |
| | | | 51.64 | 2.60 | 13.46 | 10.89 | 0.19 | 7.46 | 10.98 | 2.33 | 0.47 | 0.30 | 0.00 | bdl | 0.00 | 0.02 | 0.00 | 0.00 | 100.29 |
| | | | 50.51 | 2.62 | 13.24 | 10.82 | 0.13 | 7.29 | 10.81 | 2.28 | 0.48 | 0.29 | 0.00 | bdl | bdl | 0.04 | 0.00 | 0.00 | 98.43 |
| Internal standard of UU | ATHO-3 | | 50.83 | 2.61 | 13.13 | 10.97 | 0.15 | 7.29 | 11.01 | 2.30 | 0.48 | 0.29 | 0.01 | bdl | bdl | 0.02 | 0.00 | 0.00 | 99.00 |
| | | | 76.25 | 0.24 | 12.22 | 3.29 | 0.10 | 0.09 | 1.62 | 3.65 | 2.77 | 0.04 | 0.05 | 0.06 | 0.03 | 0.11 | 0.00 | 0.00 | 100.53 |
| | | | 75.81 | 0.24 | 12.01 | 3.32 | 0.10 | 0.10 | 1.62 | 3.55 | 2.76 | 0.02 | 0.03 | 0.04 | 0.08 | bdl | 0.00 | 0.00 | 99.63 |
| | | | 75.50 | 0.26 | 12.08 | 3.39 | 0.10 | 0.11 | 1.63 | 3.69 | 2.68 | 0.00 | 0.03 | 0.08 | 0.05 | 0.07 | 0.00 | 0.00 | 99.67 |

EPMA analysis of crystal lattice of clean fraction of quartz veins grain of Rursee samples (wt.%).

| | Veins generation | Grain ID | SiO ₂ | TiO ₂ | Al ₂ O ₃ | FeO | MnO | MgO | CaO | Na ₂ O | K ₂ O | P ₂ O ₅ | Cl | F | BaO | ZrO ₂ | O | H ₂ O | TOTAL |
|---------------------|------------------------|----------|------------------|------------------|--------------------------------|------|------|------|------|-------------------|------------------|-------------------------------|------|------|------|------------------|------|------------------|--------|
| Rursee quartz veins | Bedding Normal Veins | AH2.1_04 | 101.97 | bdl | 0.03 | 0.00 | bdl | 0.00 | bdl | 0.00 | 0.00 | bdl | 0.00 | 0.01 | 0.00 | bdl | 0.00 | | 101.91 |
| | | AH2.1_05 | 101.47 | 0.00 | bdl | bdl | 0.00 | bdl | 0.00 | 0.01 | bdl | 0.00 | 0.00 | bdl | 0.01 | 0.02 | 0.00 | | 101.38 |
| | | AH2.1_07 | 101.68 | 0.00 | 0.03 | bdl | 0.00 | 0.01 | bdl | 0.01 | 0.01 | 0.00 | 0.01 | bdl | 0.02 | bdl | 0.00 | | 101.68 |
| | | AH2.1_09 | 102.02 | bdl | bdl | bdl | 0.01 | 0.01 | bdl | bdl | 0.01 | 0.00 | bdl | bdl | 0.00 | bdl | 0.00 | | 101.89 |
| | Bedding Parallel Veins | AH2_05 | 102.67 | bdl | 0.01 | bdl | bdl | 0.00 | 0.01 | bdl | 0.00 | bdl | 0.00 | bdl | 0.01 | bdl | 0.00 | | 102.61 |
| | | AH2_06 | 102.41 | 0.02 | 0.08 | bdl | bdl | bdl | 0.00 | 0.02 | 0.01 | 0.00 | 0.00 | bdl | 0.06 | bdl | 0.00 | | 102.48 |
| | | AH2_07 | 101.69 | bdl | 0.05 | 0.00 | bdl | 0.01 | bdl | bdl | bdl | 0.01 | 0.00 | bdl | 0.00 | 0.02 | 0.00 | | 101.61 |
| | | AH2_08 | 101.42 | 0.01 | 0.03 | 0.01 | 0.00 | bdl | 0.00 | 0.00 | bdl | 0.01 | 0.01 | bdl | bdl | 0.07 | 0.00 | | 101.47 |
| | | AH2_09 | 102.34 | 0.01 | 0.04 | bdl | 0.00 | bdl | bdl | bdl | bdl | bdl | 0.00 | bdl | 0.03 | bdl | 0.00 | | 102.22 |

* bdl - below detection limit



446 5 Conclusions

- 447 • The analysis of argon isotope patterns and their interpretations (including K/Cl and inverse isochrons) indicate that
448 the main reservoir $^{39}\text{Ar}_K$ for geologically meaningful ages originated from the K-bearing minerals (illite-sericite and
449 some possible chlorite) in quartz vein microcracks and/or inclusions cavities and/or crystal lattice of quartz.
- 450 • The determination of a primary crystallization age of the quartz veins is not feasible owing to the low amount of K in
451 FIs and the high amount of excess argon within the FIAs resulting in anomalously old apparent ages in the first $\sim 20^{\text{th}}$
452 crushing steps.
- 453 • Estimates for a closure temperature for argon in K-bearing minerals inclusions is higher than the homogenization
454 temperature of FIs of quartz. However, the activity of argon diffusion within the crystal lattice of quartz is high at this
455 temperature. This may reveal that the apparent ages obtained belong to the moment of reactivation-recrystallisation
456 of veins or its cooling moment.
- 457 • The ages obtained from the quartz samples span the Jurassic-Cretaceous period. The presence of neo-crystallized
458 quartz sub-grains in the veins is due to the local tectonic activity, indicating that this period corresponds to tectonic
459 activity of the Rhenish massif.

460 Data availability

461 All data is included in the text and/or supplementary files.

462 Author contributions

463 The manuscript was primarily authored by Akbar Aydin Oglu Huseynov, the corresponding author. Co-authors Prof. Dr.
464 Klaudia F. Kuiper, Em. Prof. Dr. Jan R. Wijbrans, and Dr. Jeroen van der Lubbe made substantial contributions to data
465 interpretation and refinement of the manuscript, significantly enhancing its clarity and depth.

466 Competing interest

467 The authors declare that they have no conflict of interest.

468 Acknowledgement

469 This study has been funded by the FluidNET Consortium of EU H2020 Marie Skłodowska-Curie Action (No. 956127). We
470 would like to thank Stefan Groen for his assistance in data management and the $^{40}\text{Ar}/^{39}\text{Ar}$ analysis laboratory, as well as Roel
471 van Elsas for his help in the Mineral Separation Laboratory at VU Amsterdam. We would like to express our gratitude to



472 Bouke Lacet for preparing the epoxy grain mounts and thin sections and to Eric Hellebrand and Tilly Bouten for the EPMA
473 analysis. Finally, this study would have been impossible without the support of Prof. Dr. Janos L. Urai, who introduced us to
474 the Rursee outcrops, who unfortunately passed away.

475

476 **Supplementary file 1** Impact of blank correction on age.

477 **Supplementary file 2** K (and thus $^{40}\text{Ar}^*$) contribution from chlorite is estimated from 2D electron backscattered images.

478 **Supplementary file 3** Analytical data that have been used for $^{40}\text{Ar}/^{39}\text{Ar}$ dating.

479 **Supplementary file 4** Grain size distribution analysis of separated fluid-rich quartz fraction after crushing.

480

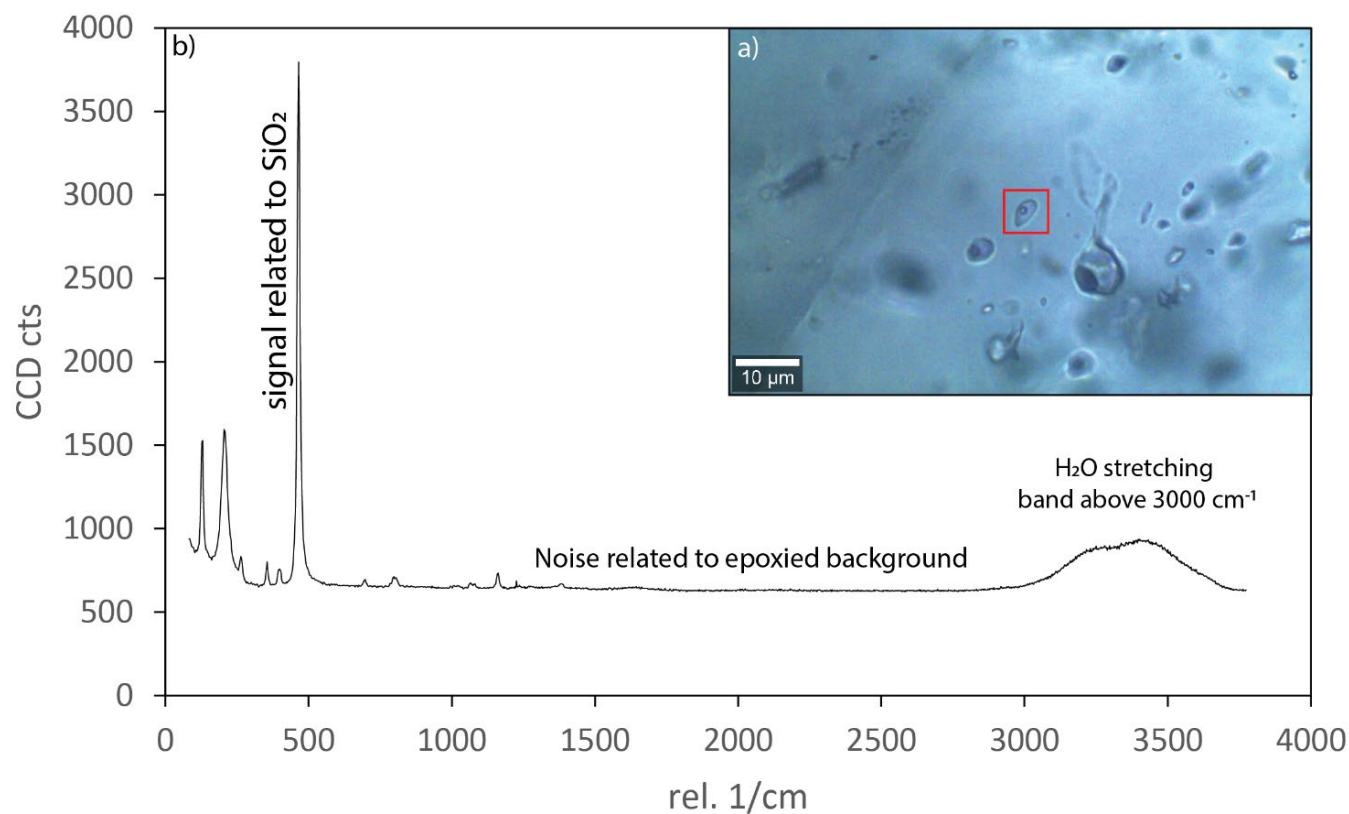
481 **Figure A1:** Raman spectroscopy of fluid inclusion from Rursee quartz veins. **(a)** Microscopic image of an epoxied and polished
482 fluid-rich quartz fraction. The fluid inclusion that underwent Raman analysis is represented by the red box. **(b)** The Raman
483 plot is presented with the wavelength on the x-axis and intensity on the y-axis. The Raman spectra shows a stretching band in
484 the wavelength range of 3000 to 3700 cm^{-1} , which indicates the presence of an aqueous system.

485 **Figure B1:** Normal isochron plots of all quartz veins samples.

486 **Table C1:** Rursee quartz veins samples J values and MDF with analytical error.



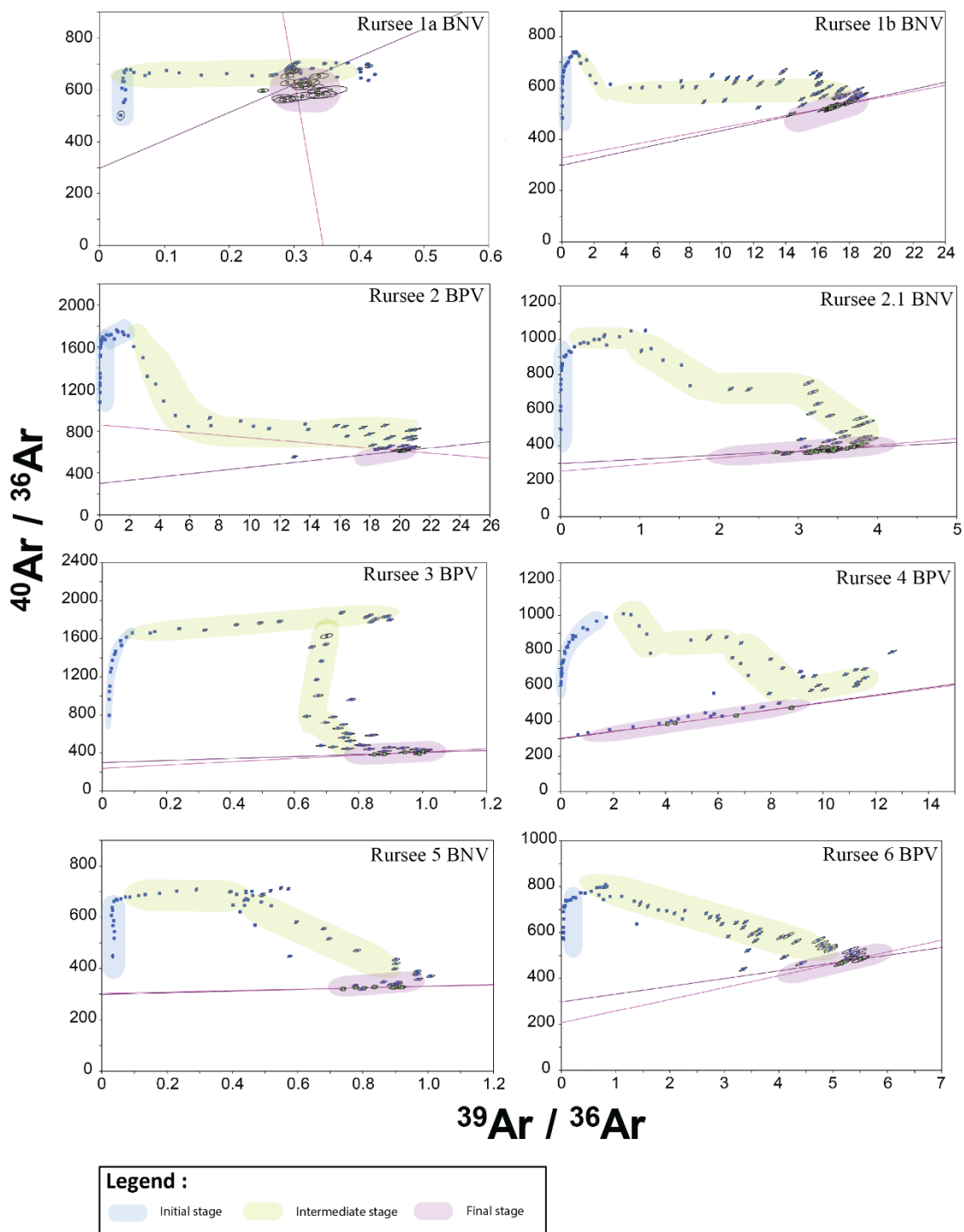
487



488 **Figure A1: Raman spectroscopy of fluid inclusion from Rursee quartz veins. (a) Microscopic image of an epoxyed and polished fluid-**
489 **rich quartz fraction. The fluid inclusion that underwent Raman analysis is represented by the red box. (b) The Raman plot is**
490 **presented with the wavelength on the x-axis and intensity on the y-axis. The Raman spectra shows a stretching band in the**
491 **wavelength range of 3000 to 3700 cm⁻¹, which indicates the presence of an aqueous system.**



492



493 **Figure B1:** Normal isochron plots of all quartz veins samples.



494 Table C1: Rursee quartz veins samples J values and MDF with analytical error.

| Sample ID | Sample ID Ar | MDF | 1 σ % | J - value | 1 σ % |
|----------------|--------------|---------|--------------|-----------|--------------|
| Rursee 1a BNV | R01a | 0.99635 | ± 0.04 | 0.0034347 | ± 0.06 |
| Rursee 1b BNV | R01b | 0.99519 | ± 0.04 | 0.0034737 | ± 0.06 |
| Rursee 2 BPV | R02 | 0.99469 | ± 0.03 | 0.0035113 | ± 0.03 |
| Rursee 2.1 BNV | R021 | 0.99492 | ± 0.03 | 0.0034868 | ± 0.04 |
| Rursee 3 BPV | R03 | 0.99868 | ± 0.03 | 0.0035113 | ± 0.03 |
| Rursee 4 BPV | R04 | 0.99749 | ± 0.03 | 0.0035113 | ± 0.03 |
| Rursee 5 BNV | R05 | 0.99494 | ± 0.04 | 0.0034868 | ± 0.04 |
| Rursee 6 BPV | R06 | 0.99709 | ± 0.04 | 0.0034868 | ± 0.04 |



495 References

- 496 Bähr, R. (1987). *Das U Th/He-System in Hämatit als Chronometer für Mineralisationen* (Ph.D. Thesis, University of
497 Heidelberg, Vol. 245, pp. 1–244).
- 498 Bai, X. J., Wang, M., Jiang, Y. D., & Qiu, H.-N. (2013). Direct dating of tin–tungsten mineralization of the Piaotang tungsten
499 deposit, South China, by $^{40}\text{Ar}/^{39}\text{Ar}$ progressive crushing. *Geochim. Cosmochim. Acta*, *114*, 1–12.
- 500 Bai, X. J., Hu, R.-G., Jiang, Y.-D., Liu, X., Tang, B., & Qiu, H.-N. (2019). Refined insight into $^{40}\text{Ar}/^{39}\text{Ar}$ progressive crushing
501 technique from K–Cl–Ar correlations in fluid inclusions. *Chemical Geology*, *515*, 37–49.
502 <https://doi.org/10.1016/j.chemgeo.2019.03.037>
- 503 Baksi, A. K. (1994). Geochronological studies on whole-rock basalts, Deccan Traps, India: Evaluation of the timing of
504 volcanism relative to the K-T boundary. *Earth and Planetary Science Letters*, *121*(1), 43–56.
505 [https://doi.org/10.1016/0012-821X\(94\)90030-2](https://doi.org/10.1016/0012-821X(94)90030-2)
- 506 Ballentine, C. J., Burgess, R., & Marty, B. (2002). Tracing fluid origin, transport and interaction in the crust.
507 <https://repository.geologyscience.ru/handle/123456789/29036>
- 508 Bambauer, H. U. (1961). Spurenelementgehalte und g-Farbzentren in Quarzen aus Zerrklüften der Schweizer Alpen.
509 *Schweizerische Mineralogische Und Petrographische Mitteilungen*, *41*, 335–369.
- 510 Baumgartner, L. P., & Ferry, J. M. (1991). A model for coupled fluid-flow and mixed-volatile mineral reactions with
511 applications to regional metamorphism. *Contributions to Mineralogy and Petrology*, *106*, 273–285.
- 512 Behr, H.-J., Horn, E. E., Frenzel-Beyme, K., & Reutel, Chr. (1987). Fluid inclusion characteristics of the Variscan and post-
513 Variscan mineralizing fluids in the Federal Republic of Germany. *Chemical Geology*, *61*(1), 273–285.
514 [https://doi.org/10.1016/0009-2541\(87\)90046-5](https://doi.org/10.1016/0009-2541(87)90046-5)
- 515 Bonhomme, M. G., Bühmann, D., & Besnus, Y. (1983). Reliability of K-Ar Dating of Clays and Silicifications Associated
516 with vein Mineralizations in Western Europe. *Geologische Rundschau*, *72*(1), 105–117.
517 <https://doi.org/10.1007/BF01765902>
- 518 Burnard, P., Graham, D., & Turner, G. (1997). Vesicle-Specific Noble Gas Analyses of ‘Popping Rock’: Implications for
519 Primordial Noble Gases in Earth. *Science*, *276*(5312), 568–571. <https://doi.org/10.1126/science.276.5312.568>
- 520 Cartwright, I., & Buick, I. S. (2000). Fluid generation, vein formation and the degree of fluid-rock interaction during
521 decompression of high-pressure terranes: The Schistes Lustres, Alpine Corsica, France. *Journal of Metamorphic
522 Geology*, *18*(6), 607–624. Scopus. <https://doi.org/10.1046/j.1525-1314.2000.00280.x>
- 523 Cartwright, J. A., Gilmour, J. D., & Burgess, R. (2013). Martian fluid and Martian weathering signatures identified in Nakhla,
524 NWA 998 and MIL 03346 by halogen and noble gas analysis. *Geochim. Cosmochim. Acta*, *105*(3), 255–293.
- 525 Chatziliadou, M., & Kramm, U. (2009). *Rb-Sr Alter und Sr-Pb Isotopencharakteristik von Gangmineralisationen in
526 paläozoischen Gesteinen am Nordrand des linksrheinischen Schiefergebirges (Raum Stolberg-Aachen-Kelmis) und*



- 527 *Vergleich mit den rezenten Thermalwässern von Aachen-Burtscheid* (RWTH-CONV-113503, Publikationsserver der
528 RWTH Aachen University). <https://publications.rwth-aachen.de/record/51191>
- 529 Cox, S. F. (2007). Structural and isotopic constraints on fluid flow regimes and fluid pathways during upper crustal
530 deformation: An example from the Taemas area of the Lachlan Orogen, SE Australia. *Journal of Geophysical*
531 *Research: Solid Earth*, 112, B08208.
- 532 Féraud, G., & Courtillot, V. (1994). Comment on: “Did Deccan volcanism pre-date the Cretaceous-Tertiary transition?” *Earth*
533 *and Planetary Science Letters*, 122(1), 259–262. [https://doi.org/10.1016/0012-821X\(94\)90068-X](https://doi.org/10.1016/0012-821X(94)90068-X)
- 534 Fielitz, W. (1995). Epizonal to lower mesozonal diastathermal metamorphism in the Ardennes (Renohercynian belt of western
535 central Europe). *Terra Nostra*, 95(8), 95.
- 536 Foland, K. A. (1983). 40Ar/39Ar incremental heating plateaus for biotites with excess argon. *Chemical Geology*, 41, 3–21.
537 [https://doi.org/10.1016/S0009-2541\(83\)80002-3](https://doi.org/10.1016/S0009-2541(83)80002-3)
- 538 Franzke, H. J., & Anderle, H.-J. (1995). Metallogeneses. In R. D. Dallmeyer, W. Franke, & K. Weber (Eds.), *Pre-Permian*
539 *Geology of Central and Eastern Europe* (pp. 138–150). Springer. https://doi.org/10.1007/978-3-642-77518-5_13
- 540 Germann, A., & Friedrich, G. (1999). Strukturkontrollierte, postvariskische Buntmetallmineralisation in paläozoischen und
541 mesozoischen Sedimentgesteinen der nordwestlichen Eifel. *Zeitschrift Der Deutschen Geologischen Gesellschaft*,
542 513–541.
- 543 Glasmacher, U., Zentilli, M., & Grist, A. M. (1998). Apatite Fission Track Thermochronology of Paleozoic Sandstones and
544 the Hill-Intrusion, Northern Linksrheinisches Schiefergebirge, Germany. In P. van den Haute & F. de Corte (Eds.),
545 *Advances in Fission-Track Geochronology: A selection of papers presented at the International Workshop on Fission-*
546 *Track Dating, Ghent, Belgium, 1996* (pp. 151–172). Springer Netherlands. [https://doi.org/10.1007/978-94-015-9133-](https://doi.org/10.1007/978-94-015-9133-1_10)
547 [1_10](https://doi.org/10.1007/978-94-015-9133-1_10)
- 548 Glasmacher, U., Tschernoster, R., Clauer, N., & Spaeth, G. (2001). K–Ar dating of magmatic sericite crystallites for
549 determination of cooling paths of metamorphic overprints. *Chemical Geology*, 175(3), 673–687.
550 [https://doi.org/10.1016/S0009-2541\(00\)00292-8](https://doi.org/10.1016/S0009-2541(00)00292-8)
- 551 Goemaere, E., & Dejonghe, L. (2005). Paleoenvironmental reconstruction of the Mirwart Formation (Pragian) in the Lambert
552 Quarry (Flamierge, Belgium). *Geologica Belgica*, 8(3), 3–14.
- 553 Götze, J., Pan, Y., & Müller, A. (2021). Mineralogy and mineral chemistry of quartz: A review. *Mineralogical Magazine*, 85(5),
554 639–664. <https://doi.org/10.1180/mgm.2021.72>
- 555 Heijlen, W., Muchez, P., & Banks, D. A. (2001). Origin and evolution of high-salinity, Zn–Pb mineralising fluids in the
556 Variscides of Belgium. *Mineralium Deposita*, 36(2), 165–176. <https://doi.org/10.1007/s001260050296>
- 557 Hein, U. F., & Behr, H. J. (1994). *Zur Entwicklung von Fluidsystemen im Verlauf der Deformationsgeschichte des*
558 *Renohercynikums*. 191–193.
- 559 Herbst, F., & Muller, H.-G. (1969). Raum und Bedeutung des Emser Gangzuges. *Gewerkschaft Mercur*.



- 560 Huseynov, A. A. O., van der Lubbe (Jeroen), H. J. L., Verdegaal-Warmerdam, S. J. A., Postma, O., Schröder, J., & Vonhof, H.
561 (2024). Novel Crushing Technique for Measuring $\delta^{18}\text{O}$ and $\delta^2\text{H}$ Values of Fluid Inclusions (H_2O) in Quartz Mineral
562 Veins Using Cavity Ring-Down Spectroscopy. *Geofluids*, 2024(1), 5795441. <https://doi.org/10.1155/2024/5795441>
- 563 IJlst, L. (1973). A laboratory overflow-centrifuge for heavy liquid mineral separation. *American Mineralogist*, 58(11–12),
564 1088–1093.
- 565 Jakobus, R. (1992). Die Erzgänge des östlichen Taunus. *Geol. Jahrb. Hess.*, 120, 145–160.
- 566 Jiang, Y. D., Qiu, H.-N., & Xu, Y. G. (2012). Hydrothermal fluids, argon isotopes and mineralization ages of the Fankou Pb-
567 Zn deposit in south China: Insights from sphalerite $^{40}\text{Ar}/^{39}\text{Ar}$ progressive crushing. *Geochim. Cosmochim. Acta*, 84,
568 369–379.
- 569 Jourdan, A.-L., Vennemann, T. W., Mullis, J., & Ramseier, K. (2009). Oxygen isotope sector zoning in natural hydrothermal
570 quartz. *Mineralogical Magazine*, 73(4), 615–632. <https://doi.org/10.1180/minmag.2009.073.4.615>
- 571 Kats, A. (1962). Hydrogen in alpha-quartz. *Philips Res. Rep.*, 17, 133–195.
- 572 Kelley, S., Turner, G., Butterfield, A. W., & Shepherd, T. J. (1986). The source and significance of argon isotopes in fluid
573 inclusions from areas of mineralization. *Earth Planet. Sci. Lett.*, 79(3–4), 303–318.
- 574 Kendrick, M. A. (2007). Comment on ‘Paleozoic ages and excess ^{40}Ar in garnets from the Bixiling eclogite in Dabieshan,
575 China: New insights from $^{40}\text{Ar}/^{39}\text{Ar}$ dating by stepwise crushing by Hua-Ning Qiu and J.R. Wijbrans’. *Geochimica*
576 *et Cosmochimica Acta*, 71, 6040–6045. <https://doi.org/10.1016/j.gca.2007.01.029>
- 577 Kendrick, M. A., & Phillips, D. (2009). Discussion of ‘the Paleozoic metamorphic history of the Central Orogenic Belt of
578 China from $^{40}\text{Ar}/^{39}\text{Ar}$ geochronology of eclogite garnet fluid inclusions by Qiu Hua-Ning and Wijbrans J.R.’ *Earth*
579 *and Planetary Science Letters - EARTH PLANET SCI LETT*, 279, 392–394.
580 <https://doi.org/10.1016/j.epsl.2008.12.047>
- 581 Kendrick, M. A., Burgess, R., Pattick, R. A. D., & Turner, P. G. (2001). Halogen and Ar–Ar age determinations of inclusions
582 within quartz veins from porphyry copper deposits using complementary noble gas extraction techniques. *Chem.*
583 *Geol.*, 177(3–4), 351–370.
- 584 Kendrick, M. A., Miller, J. M., & Phillips, D. (2006). Part II. Evaluation of ^{40}Ar – ^{39}Ar quartz ages: Implications for fluid
585 inclusion retentivity and determination of initial $^{40}\text{Ar}/^{36}\text{Ar}$ values in Proterozoic samples. *Geochim. Cosmochim.*
586 *Acta*, 70(10), 2562–2576.
- 587 Kendrick, M. A., Scambelluri, M., Honda, M., & Phillips, D. (2011). High abundances of noble gas and chlorine delivered to
588 the mantle by serpentinite subduction. *Nature Geoscience*, 4(11), 807–812. <https://doi.org/10.1038/ngeo1270>
- 589 Kirnbauer, T., Wagner, T., Taubald, H., & Bode, M. (2012). Post-Variscan hydrothermal vein mineralization, Taunus, Rhenish
590 Massif (Germany): Constraints from stable and radiogenic isotope data. *Ore Geology Reviews*, 48, 239–257.
591 <https://doi.org/10.1016/j.oregeorev.2012.03.010>
- 592 Klügel, T. (1997). Geometrie und Kinematik einer variszischen Plattengrenze. Der Südrand des Rhenoherynikums im Taunus.
593 *Geol. Abh. Hess.*, 101, 1–215.



- 594 Kołtonik, K., Pisarzowska, A., Paszkowski, M., Sláma, J., Becker, R. T., Szczerba, M., Krawczyński, W., Hartenfels, S., &
595 Marynowski, L. (2018). Baltic provenance of top-Famennian siliciclastic material of the northern Rhenish Massif,
596 Rhenohercynian zone of the Variscan orogen. *International Journal of Earth Sciences*, 107(8), 2645–2669.
597 <https://doi.org/10.1007/s00531-018-1628-4>
- 598 Koppers, A. A. P. (2002). ArArCALC—software for 40Ar/39Ar age calculations. *Computers & Geosciences*, 28(5), 605–619.
599 [https://doi.org/10.1016/S0098-3004\(01\)00095-4](https://doi.org/10.1016/S0098-3004(01)00095-4)
- 600 Korsch, R. J., & Schäfer, A. (1991). Geological interpretation of DEKORP deep seismic reflection profiles 1C and 9N across
601 the variscan Saar-Nahe Basin southwest Germany. *Tectonophysics*, 191(1), 127–146. [https://doi.org/10.1016/0040-](https://doi.org/10.1016/0040-1951(91)90236-L)
602 [1951\(91\)90236-L](https://doi.org/10.1016/0040-1951(91)90236-L)
- 603 Kučera, J., Muechez, P., Slobodník, M., & Prochaska, W. (2010). Geochemistry of highly saline fluids in siliciclastic sequences:
604 Genetic implications for post-Variscan fluid flow in the Moravosilesian Palaeozoic of the Czech Republic.
605 *International Journal of Earth Sciences*, 99(2), 269–284. <https://doi.org/10.1007/s00531-008-0387-z>
- 606 Kuiper, K. F., Deino, A., Hilgen, F. J., Krijgsman, W., Renne, P. R., & Wijbrans, J. R. (2008). Synchronizing Rock Clocks of
607 Earth History. *Science*, 320(5875), 500–504. <https://doi.org/10.1126/science.1154339>
- 608 Lee, J.-Y., Marti, K., Severinghaus, J. P., Kawamura, K., Yoo, H.-S., Lee, J. B., & Kim, J. S. (2006). A redetermination of the
609 isotopic abundances of atmospheric Ar. *Geochimica et Cosmochimica Acta*, 70(17), 4507–4512.
610 <https://doi.org/10.1016/j.gca.2006.06.1563>
- 611 Li, C., Shen, P., Li, P., Sun, J., Feng, H., & Pan, H. (2022). Changes in the factors controlling the chlorite composition and
612 their influence on hydrothermal deposit studies: A case study from Hongguleleng Manto-type Cu deposit. *Journal of*
613 *Geochemical Exploration*, 243, 107096. <https://doi.org/10.1016/j.gexplo.2022.107096>
- 614 Littke, R., Urai, J. L., Uffmann, A. K., & Risvanis, F. (2012). Reflectance of dispersed vitrinite in Palaeozoic rocks with and
615 without cleavage: Implications for burial and thermal history modeling in the Devonian of Rursee area, northern
616 Rhenish Massif, Germany. *International Journal of Coal Geology*, 89, 41–50.
617 <https://doi.org/10.1016/j.coal.2011.07.006>
- 618 Liu, J., Wu, G., Qiu, H. N., & Li, Y. (2015). 40Ar/39Ar dating, fluid inclusions and S-Pb isotope systematics of the Shabaosi
619 gold deposit, Heilongjiang Province, China. *Geol. J.*, 50(5), 592–606.
- 620 Lo, C.-H., & Onstott, T. C. (1989). 39Ar recoil artifacts in chloritized biotite. *Geochimica et Cosmochimica Acta*, 53(10),
621 2697–2711. [https://doi.org/10.1016/0016-7037\(89\)90141-5](https://doi.org/10.1016/0016-7037(89)90141-5)
- 622 Mansy, J. L., Everaerts, M., & De Vos, W. (1999). Structural analysis of the adjacent Acadian and Variscan fold belts in Belgium
623 and northern France from geophysical and geological evidence. *Tectonophysics*, 309(1), 99–116.
624 [https://doi.org/10.1016/S0040-1951\(99\)00134-1](https://doi.org/10.1016/S0040-1951(99)00134-1)
- 625 McKee, E. H., Conrad, J. E., Turrin, B. D., & Theodore, T. G. (1993). 40Ar/39Ar studies of fluid inclusions in vein quartz
626 from Battle Mountain, Nevada. *US Geological Survey Bulletin*, 2039, 155–165.



- 627 Mertz, D. F., Lippolt, H. J., & Müller, G. (1986). Isotopengeochemische (K–Ar, 40Ar/39Ar, Rb–Sr, 87Sr/86Sr) und
628 mineralogische Untersuchungen zur zeitlichen und genetischen Stellung postvariscischer Mineralisationen im Raum
629 Saar-Nahe-Pfalz. *Fortschr. Mineral.*, 64 (Beiheft 1), 116.
- 630 Min, K., Mundil, R., Renne, P. R., & Ludwig, K. R. (2000). A test for systematic errors in 40Ar/39Ar geochronology through
631 comparison with U/Pb analysis of a 1.1-Ga rhyolite. *Geochimica et Cosmochimica Acta*, 64(1), 73–98.
632 [https://doi.org/10.1016/S0016-7037\(99\)00204-5](https://doi.org/10.1016/S0016-7037(99)00204-5)
- 633 Moe, A. (2000). *Structural development of a volcanic sequence of the Lahn area during the Variscan orogeny in the*
634 *Rhenohercynian Belt (Germany)* [Dissertation]. <https://doi.org/10.11588/heidok.00001095>
- 635 Mullis, J., Dubessy, J., Poty, B., & O’Neil, J. (1994). Fluid regimes during late stages of a continental collision: Physical,
636 chemical, and stable isotope measurements of fluid inclusions in fissure quartz from a geotraverse through the Central
637 Alps, Switzerland. *Geochimica et Cosmochimica Acta*, 58(10), 2239–2267. [https://doi.org/10.1016/0016-](https://doi.org/10.1016/0016-7037(94)90008-6)
638 [7037\(94\)90008-6](https://doi.org/10.1016/0016-7037(94)90008-6)
- 639 Oliver, N. H. S., & Bons, P. D. (2001). Mechanisms of fluid flow and fluid–rock interaction in fossil metamorphic hydrothermal
640 systems inferred from vein–wallrock patterns, geometry and microstructure. *Geofluids*, 1(2), 137–162.
641 <https://doi.org/10.1046/j.1468-8123.2001.00013.x>
- 642 Oncken, O., Von Winterfeld, C., & Dittmar, U. (1999). Accretion of a rifted passive margin: The Late Paleozoic
643 Rhenohercynian fold and thrust belt (Middle European Variscides). *Tectonics*, 18(1), 75–91.
- 644 Onstott, T. C., Miller, M. L., Ewing, R. C., Arnold, G. W., & Walsh, D. S. (1995). Recoil refinements: Implications for the
645 40Ar/39Ar dating technique. *Geochimica et Cosmochimica Acta*, 59(9), 1821–1834. [https://doi.org/10.1016/0016-](https://doi.org/10.1016/0016-7037(95)00085-E)
646 [7037\(95\)00085-E](https://doi.org/10.1016/0016-7037(95)00085-E)
- 647 Ozima, M., & Podosek, F. A. (2002). *Noble gas geochemistry*. Cambridge University Press.
- 648 Pacey, A., Wilkinson, J. J., & Cooke, D. R. (2020). Chlorite and Epidote Mineral Chemistry in Porphyry Ore Systems: A Case
649 Study of the Northparkes District, New South Wales, Australia. *Economic Geology*, 115(4), 701–727.
650 <https://doi.org/10.5382/econgeo.4700>
- 651 Perny, B., Eberhardt, P., Ramseier, K., Mullis, J., & Pankrath, R. (1992). Microdistribution of Al, Li, and Na in α quartz:
652 Possible causes and correlation with short-lived cathodoluminescence. *American Mineralogist*, 77(5–6), 534–544.
- 653 Porat, N. (2006). Use of magnetic separation for purifying quartz for luminescence dating. *Ancient TL*, 24(2), 33–36.
- 654 Potrafke, A., Stalder, R., Schmidt, B. C., & Ludwig, T. (2019). OH defect contents in quartz in a granitic system at 1–5 kbar.
655 *Contributions to Mineralogy and Petrology*, 174(12), 98. <https://doi.org/10.1007/s00410-019-1632-0>
- 656 Qiu, H.-N. (1996). 40Ar–39Ar dating of the quartz samples from two mineral deposits in western Yunnan (SW China) by
657 crushing in vacuum. *Chem. Geol. (Isot. Geosci. Sect.)*, 127(1–3), 211–222.
- 658 Qiu, H.-N., & Dai, T. M. (1989). 40Ar/39Ar techniques for dating the fluid inclusions of quartz from a hydrothermal deposit.
659 *Chin. Sci. Bull.*, 34(22), 1887–1890.



- 660 Qiu, H.-N., & Jiang, Y. D. (2007). Sphalerite $40\text{Ar}/39\text{Ar}$ progressive crushing and stepwise heating techniques. *Earth Planet.*
661 *Sci. Lett.*, 256(1–2), 224–232.
- 662 Qiu, H.-N., & Wijbrans, J. R. (2006). Paleozoic ages and excess 40Ar in garnets from the Bixiling eclogite in Dabieshan,
663 China: New insights from $40\text{Ar}/39\text{Ar}$ dating by stepwise crushing. *Geochim. Cosmochim. Acta*, 70(9), 2354–2370.
- 664 Qiu, H.-N., & Wijbrans, J. R. (2008). The Paleozoic metamorphic history of the Central Orogenic Belt of China from
665 $40\text{Ar}/39\text{Ar}$ geochronology of eclogite garnet fluid inclusions. *Earth and Planetary Science Letters*, 268(3), 501–514.
666 <https://doi.org/10.1016/j.epsl.2008.01.042>
- 667 Qiu, H.-N., & Wijbrans, J. R. (2009). Reply to comment by M. A. Kendrick and D. Phillips (2009) on “The Paleozoic
668 metamorphic history of the Central Orogenic Belt of China from $40\text{Ar}/39\text{Ar}$ geochronology of eclogite garnet fluid
669 inclusions” by Hua-Ning Qiu and J. R. Wijbrans (2008) [Earth Planet. Sci. Lett. 268 (2008) 501–514]. *Earth and*
670 *Planetary Science Letters*, 279(3), 395–397. <https://doi.org/10.1016/j.epsl.2009.01.012>
- 671 Qiu, H.-N., Zhu, B., & Sun, D. (2002). Age significance interpreted from 40Ar – 39Ar dating of quartz samples from the
672 Dongchuan copper deposits, Yunnan, SW China, by crushing and heating. *Geochem. J.*, 36(5), 475–491.
- 673 Qiu, H.-N., Wu, H. Y., Yun, J. B., Feng, Z. H., Xu, Y. G., Mei, L. F., & Wijbrans, J. R. (2011). High-precision $40\text{Ar}/39\text{Ar}$ age
674 of the gas emplacement into the Songliao Basin. *Geology*, 39(5), Article 5.
- 675 Rama, S. N. I., Hart, S. R., & Roedder, E. (1965). Excess radiogenic argon in fluid inclusions. *J. Geophys. Res.*, 70(2), 509–
676 511.
- 677 Ramsay, J. G. (1986). The techniques of modern structural geology. *The Techniques of Modern Structural Geology, Folds and*
678 *Fractures*, 2, 309–700.
- 679 Rauchenstein-Martinek, K., Wagner, T., Wälle, M., & Heinrich, C. A. (2014). Gold concentrations in metamorphic fluids: A
680 LA-ICPMS study of fluid inclusions from the Alpine orogenic belt. *Chemical Geology*, 385, 70–83.
681 <https://doi.org/10.1016/j.chemgeo.2014.07.018>
- 682 Redecke, P. (1992). *Zur Geochemie und Genese variszischer und postvariszischer Buntmetallmineralisation in der Nordeifel*
683 *und der Niederrheinischen Bucht*. IML.
- 684 Schneider, J., & Haack, U. (1997). Rb/Sr dating of silicified wall rocks of a giant hydrothermal quartz vein in the SE Rhenish
685 Massif, Germany. *Proc. 4th Biennial SGA Meeting, Turku*, 971–972.
- 686 Schneider, J., Haack, U., Hein, U. F., & Germann, A. (1999). Direct Rb–Sr dating of sandstone-hosted sphalerites from
687 stratabound Pb–Zn deposits in the northern Eifel, NW Rhenish Massif, Germany. *Proc. 5th Biennial SGA Meeting*
688 *and 10th Quadrennial IAGOD Symposium, London*, 1287–1290.
- 689 Schroyen, K., & Muechez, Ph. (2000). Evolution of metamorphic fluids at the Variscan fold-and-thrust belt in eastern Belgium.
690 *Sedimentary Geology*, 131(3), Article 3. [https://doi.org/10.1016/S0037-0738\(99\)00133-5](https://doi.org/10.1016/S0037-0738(99)00133-5)
- 691 Schwab, K. (1987). Compression and right-lateral strike-slip movement at the Southern Hunsrück Borderfault (Southwest
692 Germany). *Tectonophysics*, 137(1), 115–126. [https://doi.org/10.1016/0040-1951\(87\)90318-0](https://doi.org/10.1016/0040-1951(87)90318-0)



- 693 Sintubin, M., Kenis, I., Schroyen, K., Muchez, P., & Burke, E. (2000). “Boudinage” in the High-Ardenne slate belt (Belgium),
694 reconsidered from the perspective of the “interboudin” veins. *Journal of Geochemical Exploration*, 69–70, 511–516.
695 [https://doi.org/10.1016/S0375-6742\(00\)00034-0](https://doi.org/10.1016/S0375-6742(00)00034-0)
- 696 Stalder, R., Potrafke, A., Billström, K., Skogby, H., Meinhold, G., Gögele, C., & Berberich, T. (2017). OH defects in quartz as
697 monitor for igneous, metamorphic, and sedimentary processes. *American Mineralogist*, 102(9), 1832–1842.
698 <https://doi.org/10.2138/am-2017-6107>
- 699 Sterner, S. M., Hall, D. L., & Bodnar, R. J. (1988). Synthetic fluid inclusions. V. Solubility relations in the system NaCl-KCl-
700 H₂O under vapor-saturated conditions. *Geochimica et Cosmochimica Acta*, 52(5), 989–1005.
701 [https://doi.org/10.1016/0016-7037\(88\)90254-2](https://doi.org/10.1016/0016-7037(88)90254-2)
- 702 Sumino, H., Dobrzhinetskaya, L. F., Burgess, R., & Kagi, H. (2011). Deep-mantle-derived noble gases in metamorphic
703 diamonds from the Kokchetav massif, Kazakhstan. *Earth Planet. Sci. Lett.*, 307(3–4), 439–449.
- 704 Turner, G., & Bannon, M. P. (1992). Argon isotope geochemistry of inclusion fluids from granite-associated mineral veins in
705 southwest and northeast England. *Geochim. Cosmochim. Acta*, 56(1), 227–243.
- 706 Turner, G., & Cadogan, P. H. (1974). Possible effects of ³⁹Ar recoil in ⁴⁰Ar-³⁹Ar dating. *Proceedings of the Fifth Lunar
707 Science Conference, Vol. 2, p. 1601-1615*, 5, 1601–1615.
- 708 Turner, G., & Wang, S. S. (1992). Excess argon, crustal fluids and apparent isochrons from crushing K-feldspar. *Earth Planet.
709 Sci. Lett.*, 110(1–4), 193–211.
- 710 Urai, J. L., Spaeth, G., van der Zee, W., & Hilgers, C. (2001). Evolution of mullion (boudin) structures in the Variscan of the
711 Ardennes and Eifel. *Journal of the Virtual Explorer*, 3, 1–16.
- 712 Van Noten, K., Kenis, I., Hilgers, C., Urai, J. L., Muchez, P., & Sintubin, M. (2007). Early vein generations in the High-
713 Ardenne slate belt (Belgium, Germany): The earliest manifestations of the Variscan orogeny? *Géologie de de France*,
714 2007(2), 170. <https://lirias.kuleuven.be/1929596>
- 715 Van Noten, K., Hilgers, C., L. Urai, J., & Sintubin, M. (2008). Late burial to early tectonic quartz veins in the periphery of the
716 High-Ardenne slate belt (Rursee, north Eifel, Germany). *Geologica Belgica*. [https://popups.uliege.be/1374-
717 8505/index.php?id=2485](https://popups.uliege.be/1374-8505/index.php?id=2485)
- 718 Van Noten, K., Berwouts, I., Muchez, P., & Sintubin, M. (2009). Evidence of pressure fluctuations recorded in crack-seal veins
719 in low-grade metamorphic siliciclastic metasediments, Late Palaeozoic Rhenohercynian fold-and-thrust belt
720 (Germany). *Journal of Geochemical Exploration*, 101(1), 106. <https://doi.org/10.1016/j.gexplo.2008.11.040>
- 721 Van Noten, K., Muchez, P., & Sintubin, M. (2011). Stress-state evolution of the brittle upper crust during compressional
722 tectonic inversion as defined by successive quartz vein types (High-Ardenne slate belt, Germany). *Journal of the
723 Geological Society*, 168(2), Article 2. <https://doi.org/10.1144/0016-76492010-112>
- 724 Villa, I. M. (1997). Direct determination of ³⁹Ar recoil distance. *Geochimica et Cosmochimica Acta*, 61(3), 689–691.
725 [https://doi.org/10.1016/S0016-7037\(97\)00002-1](https://doi.org/10.1016/S0016-7037(97)00002-1)



- 726 Virgo, S., Abe, S., & Urai, J. L. (2013). Extension fracture propagation in rocks with veins: Insight into the crack-seal process
727 using Discrete Element Method modeling. *J. Geophys. Res. Solid Earth*, *118*, 5236–5251.
728 <https://doi.org/10.1002/2013JB010540>
- 729 Watson, E. B., & Cherniak, D. J. (2003). Lattice diffusion of Ar in quartz, with constraints on Ar solubility and evidence of
730 nanopores. *Geochimica et Cosmochimica Acta*, *67*(11), Article 11. [https://doi.org/10.1016/S0016-7037\(02\)01340-6](https://doi.org/10.1016/S0016-7037(02)01340-6)
- 731 Weil, J. A. (1984). A review of electron spin spectroscopy and its application to the study of paramagnetic defects in crystalline
732 quartz. *Physics and Chemistry of Minerals*, *10*(4), 149–165. <https://doi.org/10.1007/BF00311472>
- 733 Wijbrans, J. R., Pringle, M. S., Koppers, A. a. P., & Scheveers, R. (1995). Argon geochronology of small samples using the
734 Vulkan argon laserprobe. *Proceedings of the Royal Netherlands Academy of Arts and Sciences*, *2*(98), 185–218.
- 735 Winterfeld, C.-H. von. (1994). Variszische Deckentektonik und devonische Beckengeometrie der Nordeifel—ein quantitatives
736 Modell. *Aachener Geowiss. Beitr*, *2*, 319.
- 737 Yardley, B. W. D. (1983). Quartz veins and devolatilization during metamorphism. *Journal of the Geological Society*, *140*(4),
738 657–663. Scopus. <https://doi.org/10.1144/gsjgs.140.4.0657>
- 739 Yardley, B. W. D., & Bottrell, S. H. (1993). Post-metamorphic gold quartz veins from NW Italy—The composition and origin
740 of the ore fluid. *Mineralogical Magazine*, *57*, 407–422.
- 741 Ziegler, P. A., & Dèzes, P. (2005). Evolution of the lithosphere in the area of the Rhine Rift System. *International Journal of*
742 *Earth Sciences*, *94*(4), 594–614. <https://doi.org/10.1007/s00531-005-0474-3>